RUFY3 and RUFY4 are ARL8 effectors that couple lysosomes to dynein-dynactin

Tal Keren-Kaplan
Eunice Kennedy Shriver National Institute of Child Health and Human Development, National Institutes of Health

Amra Saric
NIH/NICHD

Saikat Ghosh
Eunice Kennedy Shriver National Institute of Child Health and Human Development, National Institutes of Health

Chad Williamson
NIH

Rui Jia
Eunice Kennedy Shriver National Institute of Child Health and Human Development, National Institutes of Health

Yan Li
NINDS https://orcid.org/0000-0003-3820-5960

Juan Bonifacino (bonifacinoj@mail.nih.gov)
National Institutes of Health

Article

Keywords: ARL8, RUFY3, RUFY4, lysosome transport

Posted Date: May 25th, 2021

DOI: https://doi.org/10.21203/rs.3.rs-469512/v1

Version of Record: A version of this preprint was published at Nature Communications on March 21st, 2022. See the published version at https://doi.org/10.1038/s41467-022-28952-y.

RUFY3 and RUFY4 are ARL8 effectors that couple lysosomes to dynein-dynactin

Tal Keren-Kaplan[1], Amra Saric[1], Saikat Ghosh[1], Chad Williamson[1], Rui Jia[1], Yan Li[2] and Juan S. Bonifacino[1*]

[1] Neurosciences and Cellular and Structural Biology Division, *Eunice Kennedy Shriver* National Institute of Child Health and Human Development, National Institutes of Health, Bethesda, Maryland, USA.

[2] Proteomics Core Facility, National Institute of Neurological Disorders and Stroke, National Institutes of Health, Bethesda, Maryland, USA.

*Corresponding author: juan.bonifacino@nih.gov

Short title: RUFY3/4 couple lysosomes to dynein

Abstract

The small GTPase ARL8 associates with lysosomes and recruits several effectors that mediate coupling to kinesins for anterograde transport, as well as tethering for eventual fusion with other organelles. Herein we report the identification of the "RUN- and FYVE-domain-containing" proteins RUFY3 and RUFY4 as novel ARL8 effectors that couple lysosomes to dynein-dynactin for retrograde transport. Using various biochemical approaches, we find that RUFY3/4 interact with both GTP-bound ARL8 and dynein-dynactin. In addition, we show that RUFY3/4 are both necessary and sufficient for concentration of lysosomes in the juxtanuclear area of the cell. RUFY3/4 also promote retrograde transport of lysosomes in the axon of hippocampal neurons. The function of RUFY3/4 in retrograde transport is required for juxtanuclear redistribution of lysosomes upon serum starvation or cytoplasmic alkalinization, and may underlie the reported roles of RUFY3/4 in axon development/degeneration, cancer and immunity. These studies thus establish RUFY3/4 as novel ARL8-dependent, dynein-dynactin adaptors, and highlight the role of ARL8 in the regulation of both anterograde and retrograde lysosome transport.

Introduction

The ADP-ribosylation factor (ARF) family of small GTPases comprises ~30 members that regulate various aspects of cell physiology (Sztul et al., 2019). Among these members, the mammalian ARL8A and ARL8B paralogs (referred to indistinctly as "ARL8" unles otherwise specified) are unique in their ability to associate with lysosomes and to regulate multiple lysosomal functions (Khatter et al., 2015b) (for simplicity, herein we use the term "lysosomes" to denote lysosomes, late endosomes and related endosolysosomal organelles). Like other small GTPases, ARL8 cycles between GDP-bound, inactive and GTP-bound, active forms (Khatter et al., 2015b; Sztul et al., 2019). Whereas the GDP-bound form is cytosolic, the GTP-bound form associates with lysosomes (Bagshaw et al., 2006; Hofmann and Munro, 2006). The association of ARL8 with lysosomes depends on an N-terminal acetylated, amphipathic α-helix (Hofmann and Munro, 2006), which, by analogy with other members of the ARF family (Antonny et al., 1997; Liu et al., 2009), likely swings out from the rest of the molecule upon GTP binding to mediate interaction with the lipid bilayer. In addition, this association requires the lysosome-associated hetero-octameric complex BORC (Pu et al., 2015), which may function as a guanine-nucleotide-exchange factor (GEF) for the conversion of GDP-bound to GTP-bound ARL8 (Niwa et al., 2017).

The regulation of cellular functions by small GTPases is generally mediated by effectors that interact with the GTP-bound forms, resulting in recruitment and/or allosteric activation of the effectors (Sztul et al., 2019). Several effectors have been identified for mammalian ARL8, including the hetero-hexameric tethering complex HOPS (Garg et al., 2011), the adaptor proteins PLEKHM1 (Marwaha et al., 2017) and PLEKHM2 (also known as SKIP, the name used here) (Boucrot et al., 2005; Rosa-Ferreira and Munro, 2011), and the kinesin-3 motor protein KIF1 (Niwa et al., 2016). The interaction of ARL8-GTP with HOPS promotes fusion of lysosomes with late endosomes (Khatter et al., 2015a; Marwaha et al., 2017), phagosomes (Garg et al., 2011), autophagosomes (Jia et al., 2017) and Salmonella-containing vacuoles (Sindhwani et al., 2017), in some cases in cooperation with PLEKHM1 (Marwaha et al., 2017). The interaction of ARL8-GTP with SKIP mediates recruitment of the kinesin-1 motor protein ($KIF5_2$-KLC_2) for anterograde transport of lysosomes toward the peripheral cytoplasm in non-polarized cells (Guardia et al., 2016; Keren-Kaplan and Bonifacino, 2021; Pu et al., 2015; Rosa-Ferreira and Munro, 2011; Tuli et al., 2013) and the distal axon in neurons (Farias et al., 2017; Rosa-Ferreira et al., 2018; Vukoja et al., 2018). The ARL8-SKIP-kinesin-1 ensemble is also responsible for the formation of tubular lysosomes in lipopolysaccharide-treated macrophages (Mrakovic et al.,

2012) and in the process of phagolysosome resolution (Levin-Konigsberg et al., 2019). Finally, while kinesin-1 requires SKIP for interaction with ARL8-GTP, kinesin-3 interacts directly with ARL8-GTP (Niwa et al., 2016), also promoting anterograde transport of lysosomes toward the cell periphery in non-polarized mammalian cells (Guardia et al., 2016), as well as lysosomes, synaptic vesicle precursors, presynaptic active zone proteins, and dense core vesicles in *C. elegans* and Drosophila neurons (Klassen et al., 2010; Lund et al., 2021; Niwa et al., 2016; Rosa-Ferreira et al., 2018; Vukoja et al., 2018). Through these interactions, ARL8 regulates various cellular processes mediated by lysosomes (Ballabio and Bonifacino, 2020), including endocytic degradation (Khatter et al., 2015a; Oka et al., 2017), autophagy (Farias et al., 2017; Korolchuk et al., 2011; Marwaha et al., 2017; Pu et al., 2015), microbial killing and antigen presentation (Garg et al., 2011), natural killer cell cytotoxicity (Tuli et al., 2013), mTOR signaling (Jia and Bonifacino, 2019; Korolchuk et al., 2011), cell adhesion and migration (Schiefermeier et al., 2014), invasive cancer growth (Dykes et al., 2016), axonal growth-cone dynamics (Farias et al., 2017), axon branching (Adnan et al., 2020), and egress of β-coronaviruses from infected cells (Ghosh et al., 2020).

Although the number of known effectors and functions of ARL8 may seem large, there are ARF-family GTPases that have many more. For example, ARF1 has more than 15 known effectors, each of which mediates a different function (Jackson and Bouvet, 2014; Sztul et al., 2019). It is thus possible that ARL8 has an even larger set of effectors and functions than are currently known. Herein we report the results of a search for additional ARL8 effectors using MitoID (Gillingham et al., 2019), a method involving proximity biotinylation with mitochondrially-targeted forms of human ARL8A and ARL8B, followed by isolation of biotinylated proteins and mass spectrometry. Using this method, we identify the "RUN and FYVE domain-containing" proteins RUFY3 and RUFY4 (Char and Pierre, 2020) as novel ARL8 effectors. We find that ARL8 mediates recruitment of RUFY3/4 to lysosomes, promoting lysosome redistribution toward the juxtanuclear area of the cell. Moreover, we show that RUFY3/4 increase retrograde transport of lysosomes along the axon of rat hippocampal neurons. Further biochemical and cellular analyses demonstrate that RUFY3 and RUFY4 also interact with the retrograde microtubule motor dynein-dynactin, via interaction with the dynein light intermediate chain (LIC). These findings identify RUFY3 and RUFY4 as novel ARL8-dependent adaptors that couple lysosomes to dynein-dynactin for retrograde transport along microtubules. ARL8 can thus regulate both anterograde and retrograde lysosome transport through interactions with different effectors that link lysosomes to kinesin and dynein-dynactin motors, respectively.

Results

Identification of RUFY3 and RUFY4 as ARL8 effectors

To identify ARL8 effectors, we used a modification of the MitoID procedure previously developed to identify interactors of RAB GTPases (Gillingham et al., 2019) (Supplementary Fig. 1a). We attached a mitochondrial-targeting sequence (MTS) from the outer mitochondrial membrane protein TOM20 (Kanaji et al., 2000), followed by the BioID2 biotin ligase (Kim et al., 2016), to the GTP-bound (Q75L) or GDP-bound (T34N) forms of ARL8A and ARL8B lacking the N-terminal amphipathic α-helix (Mito-ARL8 constructs) (Fig. 1a). MTS-BioID2 without ARL8 was used as a negative control (Fig. 1a). The Mito-ARL8 and control constructs were expressed by transient transfection into HEK293T cells, after which cells were incubated with 50 μM biotin for 24 h. Cells were then extracted with detergent, and biotinylated proteins were captured on neutravidin-agarose beads and identified by mass spectrometry (Supplementary Fig. 1a). Data were analyzed by comparing the abundance of proteins labeled by MTS-BioID2-ARL8-Q75L relative to the MTS-BioID2 control *vs.* Mito-BioID2-ARL8-T34N relative to a Mito-BioID2 control for both ARL8A (Fig. 1b) and ARL8B (Fig. 1c) (Supplementary Dataset 1). A top hit in these analyses was the known ARL8 effector PLEKHM2 (SKIP) (Rosa-Ferreira and Munro, 2011), which was only detected in isolates from the Q75L form of both ARL8A (Fig. 1b) and ARL8B (Fig. 1c). The identification of SKIP verified the reliability of the assay.

Interestingly, another top hit for both the ARL8A (Fig. 1b) and ARL8B (Fig. 1c) constructs was a protein named RUFY3 (also known as SINGAR or ZFYVE30) (Mori et al., 2007) (Fig. 1d). RUFY3 is one of 4 members of the RUFY family of proteins in humans (Char and Pierre, 2020). These proteins comprise, in N- to C-terminal direction, RUN, coiled-coil (CC) and FYVE domains joined by disordered sequences (Fig. 1d). RUFY3, in particular, has two CC domains (CC1 and CC2) and exists as 6 spliceforms, two of which are the 620-amino-acid RUFY3.1 (transcript variant 1) (NM_001037442) (also known as RUFY3XL, (Char and Pierre, 2020) and the 469-amino-acid RUFY3.2 (transcript variant 2) (NM_014961) (Fig. 1d). Whereas RUFY3.1 includes all the domains of the RUFY family, RUFY3.2 lacks a C-terminal region comprising part of the CC2 domain and the entire FYVE domain (Fig. 1d). The shorter RUFY3.2 is the only RUFY3 spliceform characterized to date; previous studies showed that it plays roles in neuronal polarity and axon formation and degeneration (Hertz et al., 2019; Honda et al., 2017; Mori et al., 2007; Wei et al., 2014), and in cancer cell migration, invasion and metastasis (Men et al., 2019; Wang et al., 2015; Xie et al., 2017; Zhu et al., 2019). Protein and mRNA expression databases (*e.g.*, https://www.proteinatlas.org/) indicate that RUFY3 is expressed in all cells and tissues,

although with higher expression levels in the brain. Our mass spectrometric analyses identified 6 peptides derived from the longer RUFY3.1 spliceform (Supplementary Fig. 1b), demonstrating that this species is expressed in HEK293T cells.

To confirm the identification of RUFY3 as an ARL8 effector and to determine whether other members of the RUFY family also interact with ARL8, we examined the intracellular localization of GFP-tagged forms of the RUFY proteins co-expressed with MTS-BioID2-ARL8B-T34N and Mito-BioID2-ARL8B-Q75L in HeLa cells (Fig. 1e,f). We observed that, in the presence of MTS-BioID2-ARL8B-T34N, GFP-tagged RUFY1, RUFY2, RUFY3.1 and RUFY4 localized to the cytosol and to a cluster in the juxtanuclear area of the cell (Fig. 1e,f). However, in the presence of MTS-BioID2-ARL8B-Q75L, GFP-tagged RUFY3.1 and RUFY4 redistributed to mitochondria whereas GFP-tagged RUFY1 and RUFY2 retained their cytosolic/juxtanuclear distribution (Fig. 1e,f). In contrast to RUFY3.1-GFP, RUFY3.2-GFP was cytosolic (Supplementary Fig. 1c), probably because it lacks part of the CC2 and FYVE domains (Fig. 1d; see below).

To further corroborate these findings, we performed pull-down assays using recombinant GST-ARL8B proteins and FLAG-tagged RUFY proteins expressed by transient transfection in HEK293T cells (Fig. 2a). We observed that GST-ARL8B-Q75L, but not GST-ARL8B-T34N, pulled down both RUFY3.1-FLAG and RUFY4-FLAG (Fig. 2a). In contrast, neither GST-ARL8B protein pulled down RUFY1-FLAG and RUFY2-FLAG (Fig. 2a). Furthermore, we examined the co-immunoprecipitation of FLAG-tagged RUFY proteins with endogenous ARL8A and ARL8B in HEK293T cells (Fig. 2b). FLAG-tagged forms of the dynein-dynactin adaptor HOOK1 and the ARL8 effector SKIP were used as negative and positive controls, respectively. These experiments showed that RUFY3.1-FLAG and RUFY4-FLAG co-immunoprecipitated endogenous ARL8A and ARL8B, whereas RUFY1-FLAG and RUFY2-FLAG did not (Fig. 2b). Of note, the shorter RUFY3.2 showed negligible co-immunoprecipitation of ARL8A and ARL8B (Fig. 2b).

Taken together, these assays demonstrated that both RUFY3.1 and RUFY4 have the ability to interact with GTP-bound, but not GDP-bound, ARL8, suggesting that they behave as *bona fide* ARL8 effectors. RUFY1 and RUFY2, on the other hand, did not bind to any form of ARL8, ruling out their function as ARL8 effectors. Because RUFY3.2 was cytosolic and did not interact with ARL8, this spliceform was omitted from subsequent experiments, and RUFY3.1 was simply referred to as RUFY3. RUFY4 (also known as ZFYVE31) is expressed at low levels in most tissues and cells, with the exception of the brain, lung and lymphatic organs (https://www.proteinatlas.org/search/rufy4), probably explaining why it was not identified in

the MitoID experiments using HEK293T cells. Nevertheless, because it also behaves as an ARL8 effector, we performed some experiments with this protein.

The CC2 domain of RUFY3 is required for binding to ARL8

We next sought to identify the region of RUFY3 that mediates interaction with ARL8. To this end, we generated deletion constructs of RUFY3-GFP (Fig. 2c) and co-expressed them with MTS-BioID2-ARL8B-Q75L in HeLa cells (Fig. 2d). Interaction with ARL8 was inferred from re-localization of the RUFY3 constructs to mitochondria. By analogy with SKIP, which interacts with ARL8 via the RUN domain (Boucrot et al., 2005; Keren-Kaplan and Bonifacino, 2021; Rosa-Ferreira and Munro, 2011), we expected the homologous RUN domain of RUFY3 to be important. However, we found that deletion of the RUN, CC1 or FYVE domains had no effect on the re-localization of RUFY3-GFP to mitochondria (Fig. 2d,e). Likewisw, combined deletion of the RUN and CC1 domains did not prevent the re-localization of RUFY3-GFP to mitochondria (Fig. 2d,e). However, deletion of the CC2 domain, alone or in combination with the FYVE domain, abrogated re-localization of RUFY3-GFP to mitochondria (Fig. 2d,e).

In line with the mitochondrial re-localization experiments, we found that recombinant GST-ARL8B-Q75L pulled down RUFY3-FLAG constructs lacking the RUN, CC1 or FYVE domain expressed in HEK293T cells (Fig. 2f,g). In contrast, GST-ARL8B-Q75L did not pull down RUFY3-FLAG constructs lacking the CC2 domain or the CC2-FYVE tandem (Fig. 2f,g). GST-ARL8B-T34N did not pull down any of the constructs, confirming that the interactions requiring the CC2 domain are exclusive to the GTP-bound form of ARL8B.

From these experiments, we concluded that the interaction of RUFY3 with GTP-ARL8B requires the CC2 domain.

ARL8B promotes recruitment of RUFY3 and RUFY4 to a juxtanuclear cluster of vesicles

We next examined whether RUFY3 and RUFY4 co-localize with ARL8B. Because none of the antibodies we tested detect the endogenous proteins by immunofluorescence microscopy, we examined the localization of fluorescently-tagged versions of the proteins expressed by transient transfection in HeLa cells (Fig. 3a). We observed that both RUFY3-GFP and RUFY4-GFP co-localized with ARL8B-mCherry to a cluster of vesicles adjacent to the nucleus (Fig. 3a,b). Double knock out (KO) of ARL8A and ARL8B (ARL8A-B KO) shifted the distribution of RUFY3-GFP and RUFY4-GFP to the cytosol (Fig. 3c). Co-transfection of the ARL8A-B-KO cells

with ARL8B-Q75L restored the association of RUFY3-GFP and RUFY4-GFP with the juxtanuclear vesicle cluster (Fig. 3c).

To further dissect the requirement of ARL8 binding for RUFY3 recruitment to vesicles, and the domains of RUFY3 required for this recruitment, we examined the intracellular localization of the RUFY3 deletion mutants depicted in Fig. 2c. We observed that RUFY3 constructs lacking the RUN and/or CC1 domains were largely associated with the juxtanuclear cluster, whereas those lacking the CC2 or FYVE domains were more cytosolic (Fig. 3d). Combined deletion of the CC2 and FYVE domains resulted in a protein that was largely cytosolic (Fig. 3d). Thus, both the ARL8-interacting CC2 domain and the FYVE domain contribute to the localization of RUFY3 to cytoplasmic vesicles.

Taken together, the above experiments demonstrated that ARL8 promotes the recruitment of RUFY3 and RUFY4 to a juxtanuclear cluster of vesicles via the CC2 domain. The FYVE domain makes and additional contribution to this recruitment.

RUFY3 and RUFY4 promote retrograde transport of lysosomes

Because ARL8 was previously shown to associate with lysosomes (Bagshaw et al., 2006; Hofmann and Munro, 2006), we examined if the vesicles containing associated RUFY3-GFP and RUFY4-GFP also labeled for the endogenous lysosomal membrane protein LAMP1 in HeLa cells (Fig. 4a). Indeed, we observed significant co-localization of RUFY3-GFP and RUFY4-GFP with LAMP1 (Fig. 4a,b). Moreover, we noticed that cells expressing RUFY3-GFP and RUFY4-GFP exhibited more juxtanuclear clustering of lysosomes relative to cells expressing only GFP (Fig. 4c,d). Expression of the different RUFY3-GFP deletion mutants (Fig. 2c) showed that those that bound ARL8 (*i.e.*, constructs lacking the RUN, CC1 or FYVE domains) caused juxtanuclear clustering of lysosomes, whereas those that did not bind ARL8 (*i.e.*, constructs lacking the CC2 domain) failed to cause juxtanuclear clustering (Fig. 4e,f), thus demonstrating a perfect correlation between ARL8 binding and lysosome redistribution by RUFY3 and RUFY4.

Conversely, siRNA-mediated knock down of RUFY3 in HeLa cells (Fig. 4g) caused dispersal of LAMP1 toward the cell periphery (Fig. 4h-j). RUFY4 mRNA could not be detected by qRT-PCR of HeLa cells (Fig. 4g), consistent with the low expression levels of this mRNA in most cell lines (https://www.proteinatlas.org/ENSG00000188282-RUFY4/celltype). For this reason, the effect of RUFY4 knock down in these cells was not tested.

To determine if the effects of RUFY3 and RUFY4 on the distribution of lysosomes resulted from changes in lysosome transport, we examined the co-localization and movement of vesicles labeled with fluorescently-tagged RUFY3, RUFY4, ARL8B and LAMP1 in the axon and dendrites of rat hippocampal neurons in primary culture, where vesicle movement can be more readily tracked (Fig. 5). We observed that both RUFY3-FLAG and RUFY4-FLAG co-localized with a subpopulation of vesicles containing ARL8B-mCherry and LAMP1-GFP (Fig. 5a,b), as well as the endogenous lysosomal marker LAMTOR4 (Fig. 4c,d), in both the axon and dendrites. We also performed live-cell imaging and kymograph analysis of vesicle movement in the axon, where microtubules are uniformly polarized with their plus ends pointing toward the distal axon. These analyses revealed that RUFY3-GFP and RUFY4-GFP co-moved with LAMP1-RFP, mainly in the retrograde direction (*i.e.*, toward the soma) (Fig. 5e). Moreover, expression of RUFY3-GFP or RUFY4-GFP increased the proportion of retrograde *vs.* anterograde lysosomes (Fig. 5f-h) and caused an overall decrease in the number of moving lysosomes in the axon (Fig. 5g,i).

These experiments thus demonstrated that clustering of lysosomes in the juxtanuclear area of the cell by RUFY3 and RUFY4, is likely due to increased retrograde transport from the cell periphery.

RUFY3 and RUFY4 bind to dynein-dynactin

The phenotypes resulting from manipulation of RUFY3 and RUFY4 expression are consistent with these proteins playing a role in transport driven by cytoplasmic dynein-dynactin, the only microtubule motor involved in retrograde transport in the cytoplasm (Reck-Peterson et al., 2018). Indeed, we observed that both RUFY3-GFP and RUFY4-GFP co-immunoprecipitated with the endogenous dynein intermediate chain (DIC) and the endogenous $p150^{Glued}$ subunit of dynactin in HEK293T cells (Fig. 6a). In addition, purified, recombinant 6His-GFP-RUFY3 pulled down both endogenous DIC and $p150^{Glued}$ from an extract of HEK293T cells (Fig. 6b). Recombinant 6His-GFP-RUFY4 was degraded and could not be analyzed using this latter assay. Finally, we found that purified, recombinant 6His-GFP-RUFY3 could be pulled down with the purified, recombinant dynein light intermediate chain 1 (DLIC1) and, more specifically, the C-terminal domain of DLIC1 (Fig. 6c), a domain that was previously implicated in interactions with other dynein adaptors (Lee et al., 2018; Vilela et al., 2019). These results thus indicated that RUFY3 and RUFY4 interact with dynein-dynactin, and that the interaction of RUFY3 is direct via the C-terminal domain of DLIC.

To test the functional relevance of interactions of RUFY3 and RUFY4 with dynein-dynactin in cells, we compared the distribution of RUFY3-mCherry and RUFY4-mCherry in the absence or presence of overexpressed GFP-tagged CC1 domain of $p150^{Glued}$, a construct that functions as a dominant-negative inhibitor of dynein-dynactin (Quintyne et al., 1999) (Fig. 6d). We observed that, in the absence of GFP-$p150^{Glued}$-CC1, RUFY3-mCherry and RUFY4-mCherry localized to a juxtanuclear cluster, whereas in the presence of GFP-$p150^{Glued}$-CC1, RUFY3-mCherry and RUFY4-mCherry were associated with peripheral clusters, often found at cell tips (Fig. 6d). These observations demonstrated that interference with dynein-dynactin does not prevent association of RUFY3 and RUFY4 with lysosomes, but precludes their ability to move lysosomes toward the cell center.

Targeting of RUFY3 and RUFY4 to peroxisomes promotes their juxtanuclear clustering in a dynein-dependent manner

To determine whether RUFY3 and RUFY4 are sufficient for organelle coupling to dynein-dynactin, we next used a peroxisome re-localization assay (Kapitein et al., 2010). Peroxisomes are particularly suited for this assay because they are not very motile. The assay consisted of co-expressing i) a peroxisomal targeting signal from PEX3 (amino acids 1-42) fused to FKBP and RFP, together with ii) RUFY3 or RUFY4 fused to FRB and GFP (Fig. 7a). As a positive control for a known dynein-dynactin adaptor, we used a $BICD2_{25-400}$-FRB-GFP construct (Fig. 7a). Addition of rapalog brings together the FRB and FKBP domains, leading to the targeting of RUFY3 or RUFY4 to peroxisomes (Fig. 7b). We observed that, in the absence of rapalog, peroxisomes labeled with the $PEX3_{1-42}$-FKBP-RFP construct were scattered throughout the cytoplasm despite the co-expression of RUFY3-FRB-GFP, RUFY4-FRB-GFP or BICD2-FRB-GFP (Fig. 7c and e, -Rapalog). Addition of rapalog, however, resulted in the redistribution of $PEX3_{1-42}$-FKBP-RFP-labeled peroxisomes, together with RUFY3-FRB-GFP, RUFY4-FRB-GFP or BICD2-FRB-GFP, to the juxtanuclear area of the cell (Fig. 7c and e , +Rapalog). In all cases, this redistribution was blocked by knock down of the dynein heavy chain (DHC) (Fig. 7d and e, +Rapalog). These results thus demonstrated that targeting of RUFY3 or RUFY4 to an unrelated organelle is sufficient to promote its redistribution toward the cell center in a dynein-dependent manner.

RUFY3 is required for juxtanuclear redistribution of lysosomes upon serum starvation or cytoplasmic alkalinization

Removal of serum from the culture medium (i.e., "serum starvation") (Korolchuk et al., 2011; Pu et al., 2017) or cytoplasmic alkalinization (Heuser, 1989) cause redistribution of lysosomes toward the center of the cell. To determine if RUFY3 is required for these processes, we

315 performed siRNA-mediated knock down of RUFY3 in HeLa cells and examined the effect of
316 serum starvation or alkalinization on the distribution of lysosomes. We observed that both
317 manipulations caused juxtanuclear clustering lysosomes in control cells (Fig. 8a,c), but not in
318 RUFY3-knock down cells (Fig. 8b,c). These experiments thus demonstrated that the function of
319 RUFY3 in mediating dynein-dynactin-dependent transport of lysosomes is required for changes
320 in lysosome positioning in response to specific stimuli.

Discussion

At steady state, lysosomes exhibit a characteristic distribution, consisting of a densely packed population in the juxtanuclear area and a scattered population in the periphery of the cell (reviewed by (Ballabio and Bonifacino, 2020; Bonifacino and Neefjes, 2017). In polarized cells such as neurons, the peripheral population of lysosomes includes distinct pools in specialized domains of the cells (*e.g.*, axon and dendrites) (De Pace et al., 2020; Farfel-Becker et al., 2019; Farias et al., 2017; Lee et al., 2011; Tsuruta and Dolmetsch, 2015). The overall distribution of lysosomes results from the integration of various processes, including tethering to other organelles such as the endoplasmic reticulum (ER) (Jongsma et al., 2016; Raiborg et al., 2015; Rocha et al., 2009; Saric et al., 2021) and mobilization by coupling to microtubule motors (Harada et al., 1998; Hollenbeck and Swanson, 1990). Transport of lysosomes toward microtubule plus ends (*i.e.*, anterograde transport) or minus ends (*i.e.*, retrograde transport) depends on coupling to kinesin or dynein-dynactin motors, respectively (Harada et al., 1998; Hollenbeck and Swanson, 1990) (Fig. 8d). Coupling to both types of motor is not direct but mediated by small GTPases, adaptors and other effectors and regulators (Ballabio and Bonifacino, 2020; Bonifacino and Neefjes, 2017). Since there is only one cytoplasmic dynein (in contrast to the ~45 kinesins encoded in mammalian genomes), multiple combinations of adaptors and regulators allow coupling of dynein-dynactin not only to different organelles, but also to the same organelle with different functional properties. The multiple systems shown to couple lysosomes to dynein-dynactin include the small GTPase RAB7 and its effector RILP (Jordens et al., 2001), the transmembrane protein TMEM55B and adaptor protein JIP4 (Gowrishankar et al., 2021; Willett et al., 2017) , the related adaptor protein JIP3 (Drerup and Nechiporuk, 2013; Gowrishankar et al., 2021), the calcium channel MCOLN1 and penta-EF-hand protein ALG2 (Li et al., 2016), the septin protein SEPT9 (Kesisova et al., 2021), and the BLOC-1/BORC component SNAPIN (Cai et al., 2010). In the present study, we identify RUFY3 and RUFY4 as novel ARL8 effectors that couple lysosomes to dynein-dynactin (Fig. 8d).

Previous studies had characterized a short, 469-amino-acid form of RUFY3 (denoted here as RUFY3.2) that lacks part of the CC2 domain and the entire FYVE domain present in the predicted long, 620-amino-acid form of the protein (RUFY3.1) (Fig. 1d). Both forms arise by alternative splicing of the RUFY3 pre-mRNA. The short form had been shown to be particularly abundant in the brain, and to play roles in neuronal polarity and the regulation of axon specification, growth and degeneration (Hertz et al., 2019; Honda et al., 2017; Mori et al., 2007; Wei et al., 2014). The existence, distribution and function of the long form had not been

previously documented. Our MitoID procedure using ARL8A and ARL8B as baits identified RUFY3, including peptides only found in the longer RUFY3.3 form, as a top hit. This finding thus demonstrated for the first time that the longer form exists and is expressed in non-neuronal cells. Together with expression data from the Human Protein Atlas (https://www.proteinatlas.org/search/rufy3), the isolation of RUFY3.1 from HEK293T cells is consistent with the involvement of RUFY3 in non-neuronal processes such as migration, invasion and metastasis of lung, gastric and colorectal cancer cells (Men et al., 2019; Wang et al., 2015; Xie et al., 2017; Zhu et al., 2019).

The 571-amino-acid RUFY4 protein had been previously shown to be expressed mainly in lung and lymphatic organs, as well as in dendritic cells and macrophages (Men et al., 2019). The Human Protein Atlas also reports detectable expression of the RUFY4 mRNA in the brain, gastrointestinal tract and prostate (https://www.proteinatlas.org/search/rufy4), but very low levels in other tissues and cells. Functional studies revealed roles of RUFY4 in autophagosome formation, autophagosome-lysosome fusion and degradation of autophagic substrates such as damaged mitochondria and intracellular bacteria in phagocytic cells (Lassen et al., 2016; Terawaki et al., 2015).

Our findings suggest that the functions of RUFY3 in neurons and cancer cells, and RUFY4 in phagocytic cells, might be related to the ability of these proteins to couple lysosomes to dynein-dynactin. Indeed, processes such as the regulation of axonal functions (Adnan et al., 2020; Farias et al., 2017; Palomo-Guerrero et al., 2019), cancer cell migration, invasion and metastasis (Dykes et al., 2016; Schiefermeier et al., 2014; Steffan et al., 2014), and autophagy (Farias et al., 2017; Jia et al., 2017; Korolchuk et al., 2011; Marwaha et al., 2017) have all been shown to be influenced by lysosome positioning and motility, consistent with a role for RUFY3 and RUFY4 in the regulation of lysosomal functions.

Further analyses demonstrated that both RUFY3 and RUFY4 interact with the GTP-bound form of ARL8 and are recruited to lysosomes in an ARL8-dependent manner. Although ARL8 was previously shown to bind to the RUN domains of SKIP and PLEKHM1 (Farias et al., 2017; Keren-Kaplan and Bonifacino, 2021; Marwaha et al., 2017; Rosa-Ferreira and Munro, 2011), we find that binding of ARL8 to RUFY3 involves the CC2 domain of RUFY3. These observations imply that ARL8 can bind its effectors by different mechanisms. We did not dissect the ARL8-binding site on RUFY4, but there is homology to RUFY3 in the CC2 region, making it likely that both proteins interact with ARL8 in a similar manner.

Mutational dissection of RUFY3 showed that the FYVE domain also contributes to the association of RUFY3 with lysosomes. It remains to be established, however, how the RUFY3 FYVE domain contributes to these functions, since it lacks the tandem histidine residue cluster required for binding to PtdIns(3)P on endolysosomal membranes (Char and Pierre, 2020).

Despite having homology to RUFY3 in the CC2 domain and other domains, RUFY1 and RUFY2 did not interact with ARL8. Instead, RUFY1 was previously shown to interact with the small GTPases RAB4, RAB5, and RAB14, and to regulate various early endosomal functions (Cormont et al., 2001; Gosney et al., 2018; Nag et al., 2018; Vukmirica et al., 2006). RUFY2, on the other hand, was shown to interact with the Golgi complex-associated small GTPase RAB33A, which functions in autophagosome formation (Fukuda and Itoh, 2008; Fukuda et al., 2011). These interactions and functions are consistent with the differences in association of ARL8 with different RUFY family members.

In both HeLa cells and rat hippocampal neurons, transgenic RUFY3 or RUFY4 constructs co-localized with ARL8 and LAMP1 on lysosomes. Moreover, overexpression of RUFY3 or RUFY4 constructs in HeLa cells caused juxtanuclear clustering of lysosomes, and in neurons increased retrograde transport and caused depletion of lysosomes from the axon. These effects are in line with a role for RUFY3 and RUFY4 as dynein-dynactin adaptors demonstrated here. The effects in axonal transport are also in accordance with the previously reported roles of RUFY3 in neurons (Hertz et al., 2019; Honda et al., 2017; Mori et al., 2007; Wei et al., 2014). Importantly, knock down of RUFY3 in HeLa cells resulted in dispersal of lysosomes toward the cell periphery, also as expected for a dynein-dynactin adaptor. RUFY3 knock down also prevented the juxtanuclear clustering of lysosomes induced by serum starvation or cytoplasmic alkalinization. These findings indicate that RUFY3 is required for maintenance of the juxtanuclear population of lysosomes at steady-state, and for the repositioning of the peripheral population of lysosomes to the cell center in response to specific stimuli.

These findings are surprising in light of the many other proteins that were previously shown to couple lysosomes to dynein-dynactin. Why are so many dynein-dynactin adaptors involved in this process? Once possibility is that they all contribute to the overall strength of coupling. The absence of any of these adaptors could weaken the interactions of lysosomes with dynein-dynactin, tilting the balance toward interactions with kinesins and thus shifting the distribution of lysosomes to the cell periphery. The different dynein-dynactin adaptors could also have cell-type specific functions, depending on their relative expression levels. In addition, the various dynein-dynactin adaptors could be differentially regulated in response to specific stimuli, as

would be expected from their interactions with different GTPases and calcium-binding proteins. Furthermore, the adaptors could be associated with different populations of lysosomes. For simplicity, in this study we use "lysosomes" as an all-encompassing term for a variety of LAMP1-positive endolysosomal organelles. However, it is well known that LAMP1-positive organelles include functionally distinct populations of lysosomes (Johnson et al., 2016; Vukoja et al., 2018), late endosomes and even some early endosomes (Fermie et al., 2018; Saric et al., 2021). In this regard, RUFY3/4 and RILP function as dynein-dynactin adaptors for populations of endolysosomes decorated with ARL8 and RAB7, respectively (Jongsma et al., 2020). Finally, different dynein-dynactin adaptors could participate in a sequential handoff mechanism, as recently reported for the retrograde transport of maturing autophagosomes in the axon (Cason et al., 2020).

Another conundrum that remains to be solved is how ARL8 can regulate both anterograde lysosome transport of lysosomes through recruitment of kinesin-1 and kinesin-3 (Guardia et al., 2016; Rosa-Ferreira and Munro, 2011), and retrograde lysosome transport through recruitment of dynein-dynactin (this study) (Fig. 8c). Studies in Drosophila also showed that ARL8 can interact with the ortholog of RILP, a known dynein-dynactin interacting protein (Rosa-Ferreira et al., 2018). This regulation of opposing processes by the same GTPase is not exclusive to ARL8, though, since RAB7 also promotes anterograde lysosome transport via FYCO1 (Raiborg et al., 2015) and retrograde lysosome transport via RILP (Jordens et al., 2001). For both GTPases, there must be other regulators that determine the interaction with alternative adaptors and, consequently, the direction of lysosome transport. Nevertheless, the role of ARL8 in anterograde transport seems to be dominant over that in retrograde transport, since depletion of ARL8 or its positive regulator BORC cause juxtanuclear clustering of lysosomes, whereas overexpression of ARL8 drives lysosomes to the cell periphery (De Pace et al., 2020; Farias et al., 2017; Guardia et al., 2016; Keren-Kaplan and Bonifacino, 2021; Korolchuk et al., 2011; Pu et al., 2015; Rosa-Ferreira and Munro, 2011). Future studies will have to address under what conditions ARL8 promotes lysosome retrograde transport mediated by RUFY3 and RUFY4.

Our experiments using all recombinant proteins have shown that RUFY3 has the ability to bind directly to the C-terminal domain of DLIC1, a property shared with other dynein-dynactin adaptors such as BICD2, SPDL1 and HOOK1-3 (Reck-Peterson et al., 2018). As for these adaptors, the interactions could involve coiled-coil regions such as the RUFY3 CC2 domain. However, we cannot rule out the possibility that RUFY3 and RUFY4 also exert their functions indirectly, through interactions with other dynein-dynactin adaptors, perhaps providing an additional or alternative anchorage to lysosomes via ARL8. Further studies will be needed to

elucidate how the function of multiple lysosomal dynein-dynactin adaptors is integrated and how these functions are coordinated with those of kinesin adaptors to control the dynamic distribution of lysosomes under different physiological conditions.

Acknowledgements

We thank for Xiaolin Zhu and Boma Fubara excellent technical assistance, Anna Akhmanova, Brett Collins, Wade Harper, Steve Jackson, Walter Mothes, Kyle Roux and Ron Vale for kind gifts of reagents, and other members of the Bonifacino lab for helpful discussions and support. This work was supported by the Intramural Program of NICHD, NIH (project # ZIA HD001607).

Author contributions

T.K.K and J.S.B conceived the project. T.K.K designed and conducted most of the experiments. A.S. contributed reagents, conducted shell analysis of lysosome distribution and qRT-PCR. S.G. conducted and analyzed experiments in neurons. C.W. contributed to live-cell imaging and data quantification. R.J helped with experiments of lysosome repositioning. Y.L conducted mass spectrometry. T.K.K and J.S.B wrote the manuscript with input from all authors.

Materials and Methods

Recombinant DNAs

Mitochondrially-targeted ARL8 (mito-ARL8) constructs were created as follows: DNA sequences encoding the mitochondrial-targeting sequence of human TOM20 (amino acids 1-30, MVGRNSAIAAGVCGALFIGYCIYFDRKRRS) (Kanaji et al., 2000), followed by a short GAGA linker, were inserted into the pcDNA3.1-myc-BioID2-MCS plasmid (Kim et al., 2016) (a gift from Kyle Roux, Addgene #74223) by PCR to create pcDNA3.1-TOM20-myc-BioID2. Next, DNA sequences encoding human ARL8A or ARL8B lacking the N-terminal helix (amino acids 1-17) and harboring the Q75L or T34N mutations, and an N-terminally GAGA linker, were inserted into the XhoI and BamHI sites of pcDNA3.1-TOM20-myc-BioID2. The resulting plasmids encoded TOM20-GAGA-myc-BioID2-GAGA-ARL8 fusion proteins. Plasmids encoding RUFY3 deletion mutants were generated by KLD mutagenesis (Cat# M0554S, New England Biolabs) on the backbone of RUFY3-GFP and RUFY3-FLAG plasmids. The plasmid pcDNA3.1-SKIP-FOS was generated by insertion of SKIP coding sequences into the XbaI and KpnI sites of pcDNA3.1-FOS (FLAG-One-Strep). DNA sequences encoding the peroxisome-targeting sequence of PEX3 (amino acids 1-42) were cloned by KLD mutagenesis into the pEGFP-N1-SKIP$_{1\text{-}300}$-FKBP-mRFP (Keren-Kaplan and Bonifacino, 2021) vector to create pEGFP-N1-PEX3-FKBP-mRFP.

RUFY isoforms used in the study: RUFY1 isoform 1, NM_025158.5; RUFY2 isoform 1, NM_017987.4; RUFY3 isoform 1 (RUFY3.1), NM_001037442.4; RUFY3 isoform 2 (RUFY3.2), NM_014961.5; RUFY4 isoform 1, NM_198483.3. pcDNA3.1+/C-(K)-DYK-RUFY-FLAG plasmids OHu19866D, OHu02933D, OHu24594D, OHu24610D, OHu55786D, respectively, were purchased from GenScript Biotech. These plasmids were used to create plasmids encoding RUFY-GFP and RUFY-mCherry constructs by amplifying RUFY coding sequences and inserting them into EcoRI-digested pEGFP-N1 and pmCherry-N1 plasmids, respectively, by Gibson assembly (Bordat et al., 2015).

To create a pEGFP-N1-RUFY3-FRB-EGFP, a pEGFP-N1-SKIP$_{1\text{-}300}$-FRB-EGFP plasmid was digested with SalI and AgeI and the fragment containing the FRB coding sequence was cloned into pEGFP-N1-RUFY3-GFP digested with the same enzymes. To create a pEGFP-N1-RUFY4-FRB-EGFP plasmid, pEGFP-N1-SKIP$_{1\text{-}300}$-FRB-EGFP was digested with XhoI and SalI and the fragment containing the FRB coding sequence was cloned into pEGFP-N1-RUFY4-EGFP digested with the same enzymes. A BICD2 fragment encoding amino acids 25-400 was

amplified by PCR from pEGFP-N1-PEX3*-SBP-GFP (Guardia et al., 2019) (Addgene #120174), digested with BamHI and SalI, and ligated into pEGFP-N1-SKIP$_{1-300}$-FRB-EGFP digested with BglII and SalI. To create pET28a-6His-sfGFP-RUFY3.1, the coding sequences of RUFY3.1 were amplified by PCR and inserted into KpnI and NotI double-digested pET28a-6His-sfGFP-BICD2 (to replace the BICD2 with RUFY3) by Gibson assembly. To creat the pEGFP-C1-p150^{Glued}-CC1 the region encoding CC1 (amino acids 205-540) domain from chicken was cloned into the pEGFP-C1 plasmid between and EcoRI and SalI sites.

Other plasmids used in our study were: pMSCV-N-HA-FLAG-HOOK1 (gift from Wade Harper), pLAMP1-RFP (gift from W. Mothes Addgene #1817), pEGFP-N1-LAMP1-EGFP (Farias et al., 2017) and pEGFP-C1-FLAG (Britton et al., 2013) (a gift from Steve Jackson, Addgene# 46956), GFP-BICD2 (a gift from Anna Akhmanova), pET28a-6His-sfGFP-BICD2, GST-DLIC1 and GST-DLIC1-CT (gifts from Ron Vale (Schroeder et al., 2014), pOPINE-GFPnanobody (Kubala et al., 2010) (a gift from Brett Collins, Addgene #49172). All plasmids sequences were verified by Sanger sequencing (Genewiz or Eurofins Genomics).

Cell culture and treatments

HeLa and HEK293T cells (ATCC) were maintained in Dulbecco's Modified Eagle's Medium (DMEM) (Cat# 112-319-101, Quality Biological) with 10% fetal bovine serum (35-011-CV, Corning), 50 U/mL penicillin, 50 µg/mL streptomycin (Cat# 30002-CL, Corning) (CDMEM) and incubated in 5% CO_2 and 37 °C. Lipofectamine 2000 (Cat# 11668019, Thermo Fisher) was used for transfections according to manufacturer's protocol. Briefly, for immunofluorescence microscopy and live-cell imaging, 0.1-0.5 µg plasmid with 1 µl lipofectamine was used for transfection in 24-well and live-cell imaging chambers. Transfection mixture in Opti-MEM (Cat# 31985070, Gibco) was added to wells with fresh CDMEM. Culture medium was replaced by CDMEM 1 h after transfection. Cells were fixed or imaged ~24 h after transfection. For co-immunoprecipitation experiments, 1-8 µg plasmid DNA and 25 µl lipofectamine were used per 10 cm plate. 3 mL transfection mixture in Opti-MEM was added to plates containing 12 mL fresh CDMEM. Cells were harvested ~24 h after transfection.

The following siRNAs were used in this study: non-targeting siRNA (5'-UGGUUUACAUGUCGACUAAUU-3' (Dharmacon) (labeled with phosphate at the 5'), ON-TARGETplus Human RUFY3 siRNA SMARTpool (Cat# L-020336-00-0005, Horizon Discovery), Silencer Select siRNA to DYNC1H1 (ID: s4200, Cat# 4390824, Thermo Fisher). siRNA treatments were done with Oligofectamine (Cat# 12252011, Thermo Fisher) according to manufacturer's

552 protocol. Briefly, 2.5 µl of 20 µM siRNA was used per 24-well plate, or 10 µl per 6-well plate. For
553 Fig. 4h, one shot of siRNA was used in a 48 h treatment. For Fig. 7, cells were treated with one
554 shot of siRNA and transfected with plasmids 24 h after the siRNA shot. The peroxisome
555 motility assay was carried out 24 h after transfection (a total of 48 h siRNA treatment). The cells
556 were treated with or without 0.5 µM rapalog (Cat# 635057, Takara Bio) for 1 h. For siRNA
557 experiments in Fig. 8a,b, HeLa cells were treated with the siRNAs for 96 h (2 shots of siRNA).
558 Serum starvation was performed by incubating cells in serum-free DMEM for 1 h at 37 °C.
559 Alkaline medium treatment was performed by incubating cells in complete DMEM adjusted to
560 pH 8.5 with NaOH for 1 h at 37 °C. After incubation, cells were fixed with 4% paraformaldehyde
561 for 15 min at room temperature and processed for immunofluorescence microscopy.
562
563 Cover slips and live-cell chambers were pre-coated with fibronectin (Cat#F2006, Millipore-
564 Sigma). The following plates were used in the study: 4- and 8-well live-cell chambers (Cat# C4-
565 1.5H-N, Cat# C8-1.5H-N, Cellvis), 10-cm plates (Cat# 353003, Corning), 15-cm plates (Cat#
566 353025, Corning) and 24-well plates (Cat# 353047, Corning).
567

568 **Identification of ARL8-interacting proteins by MitoID**

569 ARL8 interacting proteins were identified by MitoID (Gillingham et al., 2019; Roux et al., 2013)
570 with modifications. HEK293T cells ($5.4x10^6$) were plated on 15-cm plates (Cat# 353025,
571 Corning). The next day, cells were transfected with 50 µl Lipofectamine 2000 (Cat# 11668019,
572 Thermo Fisher Scientific) and 25 µg plasmid encoding Mito-ARL8 constructs and Mito-BioID2
573 as a negative control (Fig. 1a). We prepared two 15-mL tubes with Opti-MEM; one was mixed
574 with the DNA and the second with Lipofectamine 2000. After 5-min incubation at room
575 temperature, the contents of the tubes were combined, and the mix incubated at room
576 temperature for an additional 20 min. The 6 mL mix was added to the plates containing the cells
577 that were filled with 24 mL of fresh, prewarmed CDMEM supplemented with MycoZap Plus-
578 CL (Cat# VZA-2011, Lonza). At 22 h after transfection, 50 µM biotin (Cat# 47868, Millipore-
579 Sigma) was added to each plate (1.5 mL from 1 mM stock). 24 h after biotin addition, cells were
580 scraped from the plate with 4 mL cold PBS and washed 3 times with centrifugation for 5 min, at
581 4 °C, 500 x *g*. Cell pellets were kept at -80 °C. Two plates were used for each condition. The
582 experiment was done with 3 biological replicates and all samples were processed
583 simultaneously. Thawed cells were resuspended in 5 mL buffer A (25 mM Tris-HCl pH 7.4, 150
584 mM NaCl, 1 mM EDTA 1% Triton X-100) supplemented with protease inhibitor tablet (Cat#
585 1836170, Roche). The two plates corresponding to the same condition were combined at this

stage and incubated for 1 h, at 4 °C with gentle rotation. The soluble fraction was separated by centrifugation for 20 min at 4 °C, 17,000 x *g*. A neutravidin-agarose slurry (Cat# 29201, Pierce™ NeutrAvidin™ Agarose) (500 µl, corresponding to 250 µl beads) was washed in 14 mL buffer A. The supernatant was incubated with the neutravidin-agarose overnight at 4 °C with gentle rotation. The beads were separated from the lysate by centrifugation for 5 min at 500 x *g* and 4 °C, and washed twice in 3 mL buffer B (2 % SDS), 3 times in 5 mL buffer C (0.1% deoxycholic acid, 1% Triton X-100, 1 mM EDTA, 0.5 M NaCl, 50 mM HEPES pH 7.5), and once in 5 mL 50 mM Tris-HCl pH 7.4, 50 mM NaCl. Between washes, samples were centrifuged for 5 min at 4 °C, 500 x *g*. Lastly, the washed neutravidin-agarose was resuspended in 75 µl 4X Laemmli buffer (Cat# 1610747, Bio-Rad) and samples were heated for 10 min at 99 °C. 60 µl were loaded onto 12% TGX precast gels (Cat# 4561043, Bio-Rad), which were run for a few minutes to allow the sample to enter the gel.

Mass spectrometry

Bands containing the entire sample were cut from the gel. Samples were reduced with 10 mM TECP for 1 h, alkylated with 10 mM NEM for 10 min, and digested with trypsin at 37 °C overnight. Peptides were extracted from the gel and desalted using Oasis HLB µElution plates (Waters). Digests of each sample were injected into an Ultimate 3000 RSLC nano HPLC system (Thermo Fisher). Peptides were separated on an ES802 column over a 63-min gradient with mobile phase B (98% acetonitrile, 1.9% H_2O, 0.1% formic acid) increased from 3% to 24%. LC-MS/MS data were acquired on an Orbitrap Lumos mass spectrometer (Thermo Fisher Scientific) in data-dependent acquisition mode. The MS1 scans were performed in Orbitrap with a resolution of 120K, a mass range of 375-1500 m/z, and an AGC target of 2×10^5. The quadrupole isolation was used with a window of 1.5 m/z. The MS/MS scans were triggered when the intensity of precursor ions with a charge state between 2 to 6 reached 1×10^4. The MS2 scans were conducted in ion trap. The CID method was used with collision energy fixed at 30%. The instrument was run in top speed mode. MS1 scan was performed every 3 sec, and as many MS2 scans were acquired within the 3 sec cycle. Database search and label-free quantification were performed using Proteome Discoverer 2.2 software. Up to 2 missed cleavages were allowed for trypsin digestion. NEM on cysteines and oxidation on methionine were set as fixed and variable modifications, respectively. Mass tolerances for MS1 and MS2 scans were set to 5 ppm and 0.6 Da, respectively. The search results were filtered by a false discovery rate of 1% at the protein level. The summed intensity of the unique peptides was used for protein ratio calculation. The missing values were imputed. The maximum and minimum fold changes allowed were set to 100 and 0.01 respectively. The total peptide amount of each sample was

used for normalization. The individual protein ANOVA method was used for hypothesis test. Proteins with log2 fold change ≥ 1 or ≤ -1, and adjusted p≤ 0.05 were considered significantly changed.

Antibodies

Primary antibodies: FLAG-HRP (Cat# A8592, RRID:AB_439702, mouse, 1:5,000-1:6,000, Millipore-Sigma), ARL8A (Cat# 17060-1-AP, RRID:AB_2058998, rabbit, 1:500, Proteintech), ARL8B (Cat# C13049-1-AP, RRID:AB_2059000, rabbit, 1:500, Proteintech), TOM20 (Cat# 11802-1-AP, RRID:AB_2207530, rabbit, 1:500, Proteintech), BioID2 (Cat# BID2-CP-100, chicken, 1:2000, BioFront Technologies), p150-glued (Cat# 610473, RRID:AB_397845, mouse, 1:300, BD Biosciences), DIC (Cat# MAB1618, RRID: AB_224605, mouse,1:200, Millipore-Sigma), Streptavidin-HRP (Cat# 21130, 1:10,000, Pierce), GFP-HRP (Cat# 130-091-833, RRID:AB_247003 mouse, 1:2,000, Miltenyi Biotec), LAMTOR4 (C7orf59) (D4P6O) (Cat# 13140, RRID:AB_2798129, rabbit, 1:200, Cell Signaling Technology), LAMP1 ([H4A3], DSHB Hybridoma Product H4A3, mouse, 1:500 deposited by J.T. August and J.E.K. Hildreth). FLAG (Cat# F1804, mouse, 1:200, Millipore-Sigma Sigma).

Secondary antibodies: HRP-conjugated goat anti-rabbit IgG (H+L), (Cat# 111-035-003, RRID:AB_2313567, 1:10,000 Jackson ImmunoResearch), HRP-conjugated donkey anti-mouse IgG (H+L) (Cat# 715-035-150, RRID:AB_2340770,1:10,000 Jackson ImmunoResearch), donkey-anti-mouse IgG Alexa Fluor 488 (Cat# A21202, 1:2,000, Thermo Fisher), donkey-anti-mouse IgG Alexa Fluor 555 (Cat# A31570, 1:2000, Thermo Fisher), Alexa Fluor 546-phalloidin (Cat# A22283, 1:2000, Thermo Fisher), goat anti-Chicken IgY (H+L) Alexa Fluor 555 (Cat# A21437, 1:1000, Thermo Fisher), donkey anti-mouse IgG Alexa Fluor 647 (Cat# A31571, RRID:AB_162542, 1:1,000, Thermo Fisher)

Immunofluorescence microscopy

Cells were washed 3 times with PBS, fixed with 4 % paraformaldehyde (PFA) for 15 min at room temperature, washed 3 times with PBS, incubated with PBS supplemented with 0.1 % saponin and 0.5-1 % BSA for 30 min at room temperature (blocking buffer), incubated with primary antibodies that was diluted in blocking buffer, for 30 min at 37 °C, washed 3 times with PBS, incubated with secondary antibodies diluted in blocking buffer for 30 min at 37 °C, washed twice with PBS and once with distilled water, and mounted on slides using Fluoromount-G with DAPI (Cat# 0100-20, Electron Microscopy Sciences). Alexa Fluor 546-phalloidin was added

for 15 min at room termpature, after secondary antibody was removed and coverslip was washed 3 time in PBS.

Image acquisition

Images were acquired on a Zeiss LSM780 or Zeiss LSM880 inverted confocal laser scanning microscopes fitted with a Plan-Apochromat 63X, 1.4 numerical aperture (NA) objective (Carl Zeiss). Live-cell imaging was performed in a controlled chamber (37 °C and 5 % CO_2). Z-stacks were obtained, and maximal intensity projections were generated. Images were further processed in ImageJ (Schneider et al., 2012).

Lysosome positioning measurements

To quantify lysosome positioning (Figs. 4d,f,i,j and 8c), we applied a "shell analysis"(Saric et al., 2021). Briefly, z-stack confocal fluorescence micrographs of cells immunostained for LAMP1 were flattened and a threshold was applied to eliminate background. Cells with a relatively centered nucleus and uniform shape were selected for the analysis, as narrow, elongated cells, could not be accurately quantified. These criteria were pre-defined and applied to all conditions. Cells meeting these criteria were manually traced in ImageJ/Fiji using either cytosolic GFP signal or phalloidin-stained cortical actin for visualization. The total area corresponding to LAMP1 signal in the cell was measured. Then, the cell outlines were consecutively reduced in size by a fixed length a total of 5 times, and the LAMP1 area scored each time. Such an approach resulted in 5 shells within the cell with shell 1 covering the cell vertices and shell 5 the perinuclear region. The LAMP1 signal area within shell 5 was calculated as a percentage of total LAMP1 area to give the percent perinuclear LAMP1 signal. The LAMP1 signal area within shell 1 was calculated as a percentage of total LAMP1 area to give the percent peripheral LAMP1 signal (Fig. 4j).

Co-localization analysis

Co-localization analysis (Fig.3c,4b) was done using the Pearson-Spearman correlation (PSC) plug-in for ImageJ/Fiji (Schneider et al., 2012) Scatter plots of co-localization report the Pearson's correlation coefficient (French et al., 2008), representing the relationship of the signal intensity from green (overexpression of GFP or GFP-RUFY constructs) and red (endogenously labeled LAMP1 or ARL8B-mCherry) channels of analyzed images. This value can range from -1 to +1, where 0 indicates no relationship and -1 and +1 indicate strong negative or positive correlation, respectively. The plugin allowed masking of areas to be included in the analysis. In

a given image, individual cells were masked prior to analysis using the selection brush tool as described (French et al., 2008) to determine the Pearson's correlation coefficient per cell of GFP and LAMP1 or ARL8B-mCherry signals. A threshold level of 10 was set, under which pixel values were considered noise and not included in the statistical analysis. Three experimental replicates were done. The mean Pearson's correlation coefficient per cell from each replicate experiment was plotted, and statistical significance between conditions was determined using one-way ANOVA or unpaired Student's t-test with multiple comparisons to the GFP control (n=3).

Manual scoring of microcopy experiments

Scoring of cells in which RUFY proteins localized to mitochondria (Figs. 1f, 2e) was done by visually scoring cells based on the RUFY-GFP signal (a minimum of 300 cells per condition from a total of 3 independent experiments). Scoring of peroxisome distribution (Fig. 7e) was done by visually scoring cells based on the peroxisome phenotype that was detected by the RFP signal of the $PEX3_{1-42}$-FKBP-RFP plasmid for juxtanuclear, partially juxtanuclear and dispersed peroxisomes (a minimum of 300 cells per condition from a total of 3 independent experiments were scored, except for the BICD2 construct in the NT siRNA +Rapalog condition in which 200 cells from 2 experiments were used for the analysis).

Co-immunoprecipitation

$2.5x10^6$ HEK293T cells were plated on 10-cm dishes and transfected the following day. Following transfection, cells were scraped and washed 3 times in cold PBS for 5 min at 4 °C with a 500 x *g* spin between washes. Cell pellets were resuspended in 1 mL cold lysis buffer and incubated for 30 min at 4 °C with gentle rotation. In Fig. 2b, buffer composition was: 25 mM Tris-HCl pH 7.4, 0.15 M NaCl, 1 mM EDTA, 1% NP-40 (Cat# 011332473001, Roche), 5 % glycerol, supplemented with complete EDTA-free protease inhibitor capsule (Cat# 1836170, Roche). Following lysis, the soluble fraction was separated by centrifugation for 10 min at 4 °C, 17,000 x *g*. Lysates were incubated on 20 µl magnetic-FLAG-agarose (Cat# A36797, Thermo Fisher) overnight at 4 °C with gentle rotation. Following incubation, cells were washed 3 times in 1 mL of 25 mM Tris-HCl pH 7.5, 150 mM NaCl, 0.05 % Tween-20 for 5 min at 4 °C, with a 500 x *g* spin between washes. Washed beads were eluted by addition of Laemmli sample buffer and heating for 10 min at 99 °C.

In Fig. 6a, lysis buffer composition was 25 mM HEPES pH 7.4, 1 mM DTT, 0.2 % NP-40, 0.5 mM Mg-ATP, 1 mM EGTA, 10 % glycerol, 2 mM magnesium acetate, 50 mM potassium acetate,

supplemented with complete EDTA-free protease inhibitor capsule. Lysates were incubated with 30 µl magnetic-GFP trap (homemade, detailed below) at 4 °C, 2 h with gentle rotation. Following incubation, cells were washed with lysis buffer without complete EDTA-free protease inhibitor capsule.

Real-time qRT-PCR

To determine knock-down efficiency, we used quantitative reverse transcription PCR (qRT-PCR). Briefly, total RNA was extracted from cells treated with non-targeting siRNA (siNT) or siRNA targeting RUFY3 or RUFY4, using the RNeasy Mini Kit (Cat# 74106, Qiagen) according to manufacturer's instructions. Complementary DNA was generated by reverse transcription using the Superscript VILO cDNA Synthesis Kit (11754050, Thermo Fisher), using 50 ng of the extracted mRNA as template. The cDNA was diluted 1:100 in PCR-grade water and used as template for qPCR with TaqMan® Gene Expression assays (Thermo Fisher) targeting either human RUFY3 (Cat# 4448892, Hs01127885_m1) , RUFY4 (Cat# 4448892, Hs01651015_m1) or the housekeeping gene ACTB (Cat# 4448489, Hs01060665_g1) in the TaqMan Fast Advanced Master Mix (Cat# 4444557, Thermo Fisher). qPCR was performed on the AriaMx Real-Time PCR system using the AriaMx software version 1.3 (Agilent Technologies)

Preparation of rat hippocampal neurons

Rat hippocampal neurons were isolated as previously described (Farias et al., 2016). Briefly, E18 rat embryos were harvested and euthanized. The brains were isolated in Hank's medium, and hippocampi were dissociated mechanically with a narrow-mouth glass pipette followed by trypsinization with 0.25% trypsin (Cat# 1509046, Gibco) for 15 min at 37 °C. Cells were plated on 18-mm microscopic glass coverslips coated with polylysine (Cat# 11243217001, Roche) and laminin (5 µg/mL) (Cat# P2636, Millipore-Sigma) in DMEM with 4.5 g/L glucose, 25 mM HEPES, 10% heat-inactivated horse serum (Cat# 26050-088, Gibco), 100 U/mL penicillin and 100 µg/mL streptomycin. Three hours post plating, the medium was replaced with Neurobasal medium (Cat# 21103-049, Gibco), supplemented with 1X B27 (Cat# 17504044, Thermo Scientific), Glutamax (Cat# 35050-61, Life Technologies), and 100 U/mL penicillin-streptomycin (Cat# 15140148, Gibco) and placed at 37°C and 5% CO_2.

Transfection and immunofluorescence microscopy of neurons

Rat hippocampal neurons were transfected at Day-*in-vitro* 4 (DIV4) using 1.2 µL Lipofectamine 2000 mixed in 200 µL of Opti-MEM with 1-2 µg plasmid DNA per 18-mm cover glass with 800

µL Neurobasal medium for 1 h at 37 °C. After 1 h, Lipofectamine 2000 was washed with Neurobasal medium and the cells were kept in fresh, complete Neurobasal medium for 24 h. For immunofluorescence microscopy, neurons were fixed with 4% PFA in PBS supplemented with 4% sucrose, 0.1 mM $CaCl_2$ and 1 mM $MgCl_2$ (PBS-CM) for 20 min. Cells were permeabilized with 0.2% v/v Triton X-100 for 15 min at room temperature. After that, cells were incubated with 0.2% gelatin in PBS-CM for 30 min. Primary and secondary antibodies were prepared in blocking solution and incubated for 30 min each at 37 °C. Cells were mounted with Fluoromount G (Electron Microscopy Sciences). Images were taken in a Zeiss LSM 780 confocal microscope using a Plan Apochromat 63x objective (N.A. 1.40).

Live imaging of neurons

To analyze lysosome movement, neurons were co-transfected at DIV4 with plasmids encoding RUFY3-GFP or RUFY4-GFP along with LAMP1-RFP and imaged 24 h post-transfection. In live neurons, axons were identified by labeling with CF640R (Biotium)-conjugated antibody to the axon initial segment (AIS) protein neurofascin (Farias et al 2016). Videos were recorded at 200 milliseconds for individual channels without any delay for a total of 5 min. Live-cell imaging was performed on a spinning-disk Eclipse Ti Microscope System (Nikon) equipped with a humidified environmental chamber maintained at 37 °C and 5% CO_2. Images were acquired with NIS-Elements AR microscope imaging software using a high-speed EMCCD camera (iXon Life 897, Andor). Axonal kymographs were generated using Fiji software with segmented line tool of one-pixel thickness along a segment of the axon just distal to the AIS, followed by stack re-slicing projection.

Expression and purification of recombinant proteins

BL21-CodonPlus (DE3) RP *E. coli* cells (Cat# 230255, Agilent Technologies) expressing target proteins were grown in 1 L Terrific Broth supplemented with 34 µg/mL chloramphenicol (C-6378, Millipore-Sigma) and 100 µg/mL ampicillin (Cat# A1066, Millipore-Sigma) for GST-plasmids or 30 µg/mL kanamycin (Cat# K1377, Millipore-Sigma) for 6His-sfGFP plasmids. Cultures were grown for 6-8 h at 37 °C, with 200 rpm rotation, induced with 1 mM IPTG (isopropyl β-D-1-thiogalactopyranoside) (Cat# I2481, GoldBio) and incubated overnight at 16-18 °C, 200 rpm. Bacterial cultures were pelleted by centrifugation for 20 min at 4 °C , 4,000 rpm. and pellets were resuspended in lysis buffer supplemented with lysozyme (Cat# VWRV0663, VWR), DNase I (Cat# LS002139, Worthington Biochemical Corporation) and complete EDTA-free protease inhibitor capsules (Cat# 1836170, Roche) (specific buffers used are listed below for

each protein purified in this study). Following sonication and centrifugation for 30-45 min at 4°C, 16,000 rpm, cleared lysates were incubated with glutathione-Sepharose 4B (Cat# 17-0756-05, Cytvia) (for GST- tagged proteins) or cOmplete-His-Tag Purification Resin (Cat# 5893682001, Roche) (for 6His-sfGFP-tagged proteins) for 1-2 h at 4 °C, with gentle end-to-end rotation.

For purification of GST-ARL8B-Q75L and -T34N, lysis buffer was 50 mM Tris-HCl pH 8.0, 150 mM NaCl, 8 mM $MgCl_2$, 5% glycerol and 5 mM β-Mercaptoethanol (Cat# M6250, Millipore-Sigma) supplemented with 100 µM GDP (Cat# G7127, Millipore-Sigma) (for GST-ARL8B-T34N) or 100 µM GTPγS (Cat# G8634, Millipore-Sigma) (for GST-ARL8B-Q75L). Bound glutathione-Sepharose was washed in buffer containing 50 mM Tris-HCl pH 8.0, 150 mM NaCl, 8 mM $MgCl_2$, 5% glycerol and 5 mM β-Mercaptoethanol (Cat# M6250, Millipore-Sigma) supplemented with 100 µM GDP (G7127, Millipore-Sigma) (for GST-ARL8B-T34N) or 100 µM GTPγS (Cat# G8634, Millipore-Sigma) (for GST-ARL8B-Q75L).

GST-DLIC1 , and GST-DLIC-CT were expressed in BL21(DE3) (Cat# C2527I, New England Biolabs) and lysis buffer was 50 mM Tris-HCl pH 8.0, 150 mM NaCl, 10% glycerol, and 1 mM DTT (Cat# DTT-RO, Roche). Following binding to glutathione Sepharose and washes, bound protein was further eluted from the glutathioneSepharose with elution buffer containing 50 mM Tris-HCl pH 8.0 and 10 mM L-glutathione. Eluant was further purified on HiLoad 16/600 Superdex 200 (Cat# 28-9893-35, Cytvia) in buffer containing 10 mM Tris-HCl pH 7.0, 50 mM NaCl, 2 mM $MgCl_2$ and 2mM Tris(2-carboxyethyl)phosphine hydrochloride (TCEP) (Cat# C4706, Millipore-Sigma). Peak fractions were pooled together, aliquoted, flash-frozen in liquid nitrogen and stored at -80 °C

For 6His-sfGFP-RUFY3, 6His-sfGFP-BICD2 and 6His-sfGFP-GFP purification, lysis buffer was 50 mM Tris-HCl pH 8.0, 300 mM NaCl, 5 % glycerol and 1 mM DTT (Cat# 10708984001, Millipore-Sigma). Bound proteins on cOmplete-His-Tag Purification Resin (Cat# 5893682001, Roche) were washed in buffer containing 50 mM Tris-HCl pH 8.0, 300 mM NaCl, 5 % glycerol and eluted in buffer composed of 50 mM Tris-HCl pH 8.0, 300 mM NaCl, 5 % glycerol with 1 mM DTT and 90 mM imidazole. Proteins were further purified on Superose 6 increase 10/300 column (Cat# 29-0915-96, Cytvia) in 50 mM Tris-HCl pH 8.0, 300 mM NaCl, 5 % glycerol and 1 mM DTT. Peak fractions were pooled together, aliquoted, flash-frozen at liquid nitrogen and stored at -80 °C.

Preparation of GFP-nanobody conjugated agarose

Homemade GFP-Trap beads were generated by first purifying the GFP nanobody, then coupling it to N-hydroxysuccinimide (NHS) beads (Cat# GE28-9513-80, Millipore-Sigma). *E.coli* BL21 (DE3) were transformed with pOPINE-GFPnanobody plasmid, (Kubala et al., 2010) (a gift from Brett Collins, Addgene #49172). GFP nanobody was expressed as described above with buffer composed of 50 mM Tris-HCl, 300 mM NaCl, 5 % glycerol and 1 mM DTT that was supplemented with DNAseI, lysozyme and complete EDTA free tablet. cOmplete His-Tag purification resin was prepared by washing 5 mL of resin with cold PBS. The cleared lysate was incubated in batch mode with the cOmplete His-Tag purification resin for 30 min at 4 °C, with end-to-end rotation. The lysate was removed, the resin washed with 600 mL cold PBS and the proteins eluted in PBS supplemented with 500 mM imidazole. The elution was conducted 4 times for a total elution volume of 20 mL. Eluant was dialyzed in 4 L PBS supplemented with 150 mM NaCl overnight at 4 °C. The nanobody was additionally purified by gel filtration on a Superdex 200 increase 300/10 column (Cat# 28-9909-44, Cytvia) in 25 mM HEPES pH 7.4, 150 mM NaCl. Peak fractions were pooled and purified nanobody at 1.8 mg/ml concentration was aliquoted, flash frozen and stored at -80°C while 1 mg was used to prepare GFP-Trap beads.

Coupling of the nanobody to NHS Mag Sepharose (Cat# GE28-9513-80, Millipore-Sigma) was conducted according to supplier's specifications. Briefly, one 500 µL tube of NHS Mag Sepharose was placed on a magnetic rack and the storage solution was removed. The beads were equilibrated by resuspending them in 500 µL ice-cold 1 M HCl and removing the liquid. The 1 mg of purified nanobody, diluted to 1 mL in 0.2 M $NaHCO_3$, 0.5 M NaCl, pH 8.3, was added to the beads and allowed to mix end-over-end at room temperature for 20 min. The nanobody solution was then removed and residual active groups were blocked by sequential washes in 50 mM Tris-HCl, 1 M NaCl, pH 8 (Buffer A) and 50 mM glycine-HCl, 1 M NaCl, pH 3.0 (Buffer B). The washes were as follows: 500 µL Buffer A, 500 µL Buffer B, 500 µL Buffer A, mixed end-over-end at room temperature for 15 min. The buffer was removed. The beads were sequentially washed in 500 µL Buffer B, 500 µL Buffer A and 500 µL Buffer B. The beads were resuspended in 500 µL of 50 mM Tris-HCl pH 7.4 containing 20% ethanol and stored at 4°C.

Pull downs

HEK293T cells expressing RUFYs or RUFY-FLAG plasmids were scraped from 10-cm plates and washed 3 times in 1 mL cold PBS followed by centrifugation for 5 min at 4 °C, 500 x *g*. Pellets were resuspended in 1 mL buffer containing 25 mM Tris-HCl pH 7.4, 150 mM NaCl, 1 mM EDTA, 1 % NP-40 (Cat# 011332473001, Roche) and 5 % glycerol, supplemented with complete

EDTA-free protease inhibitor capsule (Cat# 1836170, Roche) and 500 µM GDP (Cat# G7127, Millipore-Sigma) (for GST-ARL8B-T34N) or 500 µM GTPγS (Cat# G8634, Millipore-Sigma) (for GST-ARL8B-Q75L), 1 mM DL-Dithiothreitol (DTT) (Cat# 10708984001, Millipore-Sigma) and 8 mM $MgCl_2$,and incubated for 30 min at 4 °C with gentle rotation. Lysates were entrifuged for 10 min at 4 °C, 17,000 x g and incubated with 20 µl glutathione-Sepharose loaded with GST-ARL8B-Q75L or GST-ARL8B-T34N for 1 h at 4 °C with gentle rotation (preparation of GST-ARL8B-Q75L and -T34N is described above). Bound material was separated by centrifugation for 5 min at 4 °C, 500 x *g*, and washed 3 times with 1 mL buffer containing 50 mM Tris-HCl pH 8.0, 150 mM NaCl, 8 mM $MgCl_2$, 5% glycerol and 5 mM β-Mercaptoethanol (Cat# M6250, Millipore-Sigma) supplemented with 100 µM GDP (Cat# G7127, Millipore-Sigma) (for GST-ARL8B-T34N) or GTPγS (G8634, Millipore-Sigma) (for GST-ARL8B-Q75L) (Cat# 10708984001, Millipore-Sigma). Samples were eluted with Laemmli sample buffer for 10 min at 99 °C.

For the pull down with GST-DLIC and GST-DLIC-CT, 20 µg protein were incubated with 20 µl glutathione-Sepharose. Loaded GST-beads were incubated with 5 µg purified 6His-sfGFP-RUFY3 for 1 h at 4 °C with gentle rotation.

Endogenous dynein pulldown

We used a published protocol (Kesisova et al., 2021; McKenney et al., 2014) with modifications. HEK293T cells from fifteen 15-cm plates were scraped and washed 3 times in cold PBS for 5 min at 4 °C, 500 x *g* centrifugations between washes. Cells were lysed in 15 ml buffer composed of 25 mM HEPES pH 7.4, 5 mM DTT, 0.2 % NP40, 1 mM Mg-ATP, 1 mM EGTA, 10 % glycerol, 2 mM magnesium acetate, 50 mM potassium acetate supplemented with complete EDTA-free protease inhibitor capsule for 1 h at 4 °C with gentle rotation. The supernatant was separated by centrifugation for 30 min at 4° C and 120,000 x *g* (TLA45). 3.5 mL of the cleared HEK293T lysate was mixed with 100 µl Strep-Tactin Sepharose resin (Cat# 2-1201-010, IBA) and also 40 µg purified 6His-sfGFP-RUFY3, 6His-sfGFP-BICD2 and 6His-sfGFP and incubated over-night at 4 °C with gentle rotation. Following incubation, beads were washed 5 times in 2 mL buffer for 3 min at 4 °C and 500 x *g* spins between washes. Samples were further eluted with 50 µl 4X Laemmli sample buffer, 10 min at 99 °C.

Statistical calculations

All statistical tests were performed on n=3 independent experiments, except in Fig. 8c where 40-50 cells were analyzed per condition in one experiment. Data are presented as superplots (Lord

et al., 2020). Individual data points from each experiment are color coded and correspond to the big circles representing the average for each experiment. Error bars show standard deviation. We used One-way ANOVA when multiple groups were compared and unpaired Student's t-test when two groups were compared. Data in Figs. 4c,e,h,I were normalized to GFP. This was done to account for experiment-to-experiment variability (the trends within each experiment was always consistent).

References

Adnan, G., Rubikaite, A., Khan, M., Reber, M., Suetterlin, P., Hindges, R., and Drescher, U. (2020). The GTPase Arl8B Plays a Principle Role in the Positioning of Interstitial Axon Branches by Spatially Controlling Autophagosome and Lysosome Location. J Neurosci *40*, 8103-8118.

Antonny, B., Beraud-Dufour, S., Chardin, P., and Chabre, M. (1997). N-terminal hydrophobic residues of the G-protein ADP-ribosylation factor-1 insert into membrane phospholipids upon GDP to GTP exchange. Biochemistry *36*, 4675-4684.

Bagshaw, R.D., Callahan, J.W., and Mahuran, D.J. (2006). The Arf-family protein, Arl8b, is involved in the spatial distribution of lysosomes. Biochem Biophys Res Commun *344*, 1186-1191.

Ballabio, A., and Bonifacino, J.S. (2020). Lysosomes as dynamic regulators of cell and organismal homeostasis. Nat Rev Mol Cell Biol *21*, 101-118.

Bonifacino, J.S., and Neefjes, J. (2017). Moving and positioning the endolysosomal system. Curr Opin Cell Biol *47*, 1-8.

Bordat, A., Houvenaghel, M.C., and German-Retana, S. (2015). Gibson assembly: an easy way to clone potyviral full-length infectious cDNA clones expressing an ectopic VPg. Virol J *12*, 89.

Boucrot, E., Henry, T., Borg, J.P., Gorvel, J.P., and Meresse, S. (2005). The intracellular fate of Salmonella depends on the recruitment of kinesin. Science *308*, 1174-1178.

Britton, S., Coates, J., and Jackson, S.P. (2013). A new method for high-resolution imaging of Ku foci to decipher mechanisms of DNA double-strand break repair. J Cell Biol *202*, 579-595.

Cai, Q., Lu, L., Tian, J.H., Zhu, Y.B., Qiao, H., and Sheng, Z.H. (2010). Snapin-regulated late endosomal transport is critical for efficient autophagy-lysosomal function in neurons. Neuron *68*, 73-86.

Cason, S.E., Carman, P., Van Duyne, C., Goldsmith, J., Dominguez, R., and Holzbaur, E.L.F. (2020). Sequential dynein effectors regulate axonal autophagosome motility in a maturation-dependent pathway. bioRxiv, https://doi.org/10.1101/2020.11.01.363333

933 Char, R., and Pierre, P. (2020). The RUFYs, a Family of Effector Proteins Involved in
934 Intracellular Trafficking and Cytoskeleton Dynamics. Front Cell Dev Biol *8*, 779.

935 Cormont, M., Mari, M., Galmiche, A., Hofman, P., and Le Marchand-Brustel, Y. (2001). A FYVE-
936 finger-containing protein, Rabip4, is a Rab4 effector involved in early endosomal traffic.
937 Proc Natl Acad Sci U S A *98*, 1637-1642.

938 De Pace, R., Britt, D.J., Mercurio, J., Foster, A.M., Djavaherian, L., Hoffmann, V., Abebe, D., and
939 Bonifacino, J.S. (2020). Synaptic Vesicle Precursors and Lysosomes Are Transported by
940 Different Mechanisms in the Axon of Mammalian Neurons. Cell Rep *31*, 107775.

941 Drerup, C.M., and Nechiporuk, A.V. (2013). JNK-interacting protein 3 mediates the retrograde
942 transport of activated c-Jun N-terminal kinase and lysosomes. PLoS Genet *9*, e1003303.

943 Dykes, S.S., Gray, A.L., Coleman, D.T., Saxena, M., Stephens, C.A., Carroll, J.L., Pruitt, K., and
944 Cardelli, J.A. (2016). The Arf-like GTPase Arl8b is essential for three-dimensional
945 invasive growth of prostate cancer in vitro and xenograft formation and growth in vivo.
946 Oncotarget *7*, 31037-31052.

947 Farfel-Becker, T., Roney, J.C., Cheng, X.T., Li, S., Cuddy, S.R., and Sheng, Z.H. (2019). Neuronal
948 Soma-Derived Degradative Lysosomes Are Continuously Delivered to Distal Axons to
949 Maintain Local Degradation Capacity. Cell Rep *28*, 51-64 e54.

950 Farias, G.G., Britt, D.J., and Bonifacino, J.S. (2016). Imaging the Polarized Sorting of Proteins
951 from the Golgi Complex in Live Neurons. Methods Mol Biol *1496*, 13-30.

952 Farias, G.G., Guardia, C.M., De Pace, R., Britt, D.J., and Bonifacino, J.S. (2017). BORC/kinesin-1
953 ensemble drives polarized transport of lysosomes into the axon. Proc Natl Acad Sci U S
954 A *114*, E2955-E2964.

955 Fermie, J., Liv, N., Ten Brink, C., van Donselaar, E.G., Muller, W.H., Schieber, N.L., Schwab, Y.,
956 Gerritsen, H.C., and Klumperman, J. (2018). Single organelle dynamics linked to 3D
957 structure by correlative live-cell imaging and 3D electron microscopy. Traffic *19*, 354-
958 369.

959 French, A.P., Mills, S., Swarup, R., Bennett, M.J., and Pridmore, T.P. (2008). Colocalization of
960 fluorescent markers in confocal microscope images of plant cells. Nat Protoc *3*, 619-628.

961 Fukuda, M., and Itoh, T. (2008). Direct link between Atg protein and small GTPase Rab: Atg16L
962 functions as a potential Rab33 effector in mammals. Autophagy *4*, 824-826.

963 Fukuda, M., Kobayashi, H., Ishibashi, K., and Ohbayashi, N. (2011). Genome-wide investigation
964 of the Rab binding activity of RUN domains: development of a novel tool that
965 specifically traps GTP-Rab35. Cell Struct Funct *36*, 155-170.

966 Garg, S., Sharma, M., Ung, C., Tuli, A., Barral, D.C., Hava, D.L., Veerapen, N., Besra, G.S.,
967 Hacohen, N., and Brenner, M.B. (2011). Lysosomal trafficking, antigen presentation, and
968 microbial killing are controlled by the Arf-like GTPase Arl8b. Immunity *35*, 182-193.

969 Ghosh, S., Dellibovi-Ragheb, T.A., Kerviel, A., Pak, E., Qiu, Q., Fisher, M., Takvorian, P.M.,
970 Bleck, C., Hsu, V.W., Fehr, A.R., *et al.* (2020). beta-Coronaviruses Use Lysosomes for
971 Egress Instead of the Biosynthetic Secretory Pathway. Cell *183*, 1520-1535 e1514.

972 Gillingham, A.K., Bertram, J., Begum, F., and Munro, S. (2019). In vivo identification of GTPase
973 interactors by mitochondrial relocalization and proximity biotinylation. Elife *8*.

974 Gosney, J.A., Wilkey, D.W., Merchant, M.L., and Ceresa, B.P. (2018). Proteomics reveals novel
975 protein associations with early endosomes in an epidermal growth factor-dependent
976 manner. J Biol Chem *293*, 5895-5908.

977 Gowrishankar, S., Lyons, L., Rafiq, N.M., Roczniak-Ferguson, A., De Camilli, P., and Ferguson,
978 S.M. (2021). Overlapping roles of JIP3 and JIP4 in promoting axonal transport of
979 lysosomes in human iPSC-derived neurons. Mol Biol Cell, mbcE20060382.

980 Guardia, C.M., De Pace, R., Sen, A., Saric, A., Jarnik, M., Kolin, D.A., Kunwar, A., and
981 Bonifacino, J.S. (2019). Reversible association with motor proteins (RAMP): A
982 streptavidin-based method to manipulate organelle positioning. PLoS Biol *17*, e3000279.

983 Guardia, C.M., Farias, G.G., Jia, R., Pu, J., and Bonifacino, J.S. (2016). BORC Functions Upstream
984 of Kinesins 1 and 3 to Coordinate Regional Movement of Lysosomes along Different
985 Microtubule Tracks. Cell Rep *17*, 1950-1961.

986 Harada, A., Takei, Y., Kanai, Y., Tanaka, Y., Nonaka, S., and Hirokawa, N. (1998). Golgi
987 vesiculation and lysosome dispersion in cells lacking cytoplasmic dynein. J Cell Biol *141*,
988 51-59.

989 Hertz, N.T., Adams, E.L., Weber, R.A., Shen, R.J., O'Rourke, M.K., Simon, D.J., Zebroski, H.,
990 Olsen, O., Morgan, C.W., Mileur, T.R., *et al.* (2019). Neuronally Enriched RUFY3 Is
991 Required for Caspase-Mediated Axon Degeneration. Neuron *103*, 412-422 e414.

992 Heuser, J. (1989). Changes in lysosome shape and distribution correlated with changes in
993 cytoplasmic pH. J Cell Biol *108*, 855-864.

994 Hofmann, I., and Munro, S. (2006). An N-terminally acetylated Arf-like GTPase is localised to
995 lysosomes and affects their motility. J Cell Sci *119*, 1494-1503.

996 Hollenbeck, P.J., and Swanson, J.A. (1990). Radial extension of macrophage tubular lysosomes
997 supported by kinesin. Nature *346*, 864-866.

998 Honda, A., Usui, H., Sakimura, K., and Igarashi, M. (2017). Rufy3 is an adapter protein for small
999 GTPases that activates a Rac guanine nucleotide exchange factor to control neuronal
1000 polarity. J Biol Chem *292*, 20936-20946.

1001 Jackson, C.L., and Bouvet, S. (2014). Arfs at a glance. J Cell Sci *127*, 4103-4109.

1002 Jia, R., and Bonifacino, J.S. (2019). Lysosome Positioning Influences mTORC2 and AKT
1003 Signaling. Mol Cell *75*, 26-38 e23.

1004 Jia, R., Guardia, C.M., Pu, J., Chen, Y., and Bonifacino, J.S. (2017). BORC coordinates encounter
1005 and fusion of lysosomes with autophagosomes. Autophagy *13*, 1648-1663.

1006 Johnson, D.E., Ostrowski, P., Jaumouille, V., and Grinstein, S. (2016). The position of lysosomes
1007 within the cell determines their luminal pH. J Cell Biol *212*, 677-692.

1008 Jongsma, M.L., Bakker, J., Cabukusta, B., Liv, N., van Elsland, D., Fermie, J., Akkermans, J.L.,
1009 Kuijl, C., van der Zanden, S.Y., Janssen, L., *et al.* (2020). SKIP-HOPS recruits TBC1D15 for
1010 a Rab7-to-Arl8b identity switch to control late endosome transport. EMBO J *39*, e102301.

1011 Jongsma, M.L., Berlin, I., Wijdeven, R.H., Janssen, L., Janssen, G.M., Garstka, M.A., Janssen, H.,
1012 Mensink, M., van Veelen, P.A., Spaapen, R.M., *et al.* (2016). An ER-Associated Pathway
1013 Defines Endosomal Architecture for Controlled Cargo Transport. Cell *166*, 152-166.

1014 Jordens, I., Fernandez-Borja, M., Marsman, M., Dusseljee, S., Janssen, L., Calafat, J., Janssen, H.,
1015 Wubbolts, R., and Neefjes, J. (2001). The Rab7 effector protein RILP controls lysosomal
1016 transport by inducing the recruitment of dynein-dynactin motors. Curr Biol *11*, 1680-
1017 1685.

1018 Kanaji, S., Iwahashi, J., Kida, Y., Sakaguchi, M., and Mihara, K. (2000). Characterization of the
1019 signal that directs Tom20 to the mitochondrial outer membrane. J Cell Biol *151*, 277-288.

Kapitein, L.C., Schlager, M.A., van der Zwan, W.A., Wulf, P.S., Keijzer, N., and Hoogenraad, C.C. (2010). Probing intracellular motor protein activity using an inducible cargo trafficking assay. Biophys J *99*, 2143-2152.

Keren-Kaplan, T., and Bonifacino, J.S. (2021). ARL8 Relieves SKIP Autoinhibition to Enable Coupling of Lysosomes to Kinesin-1. Curr Biol *31*, 540-554 e545.

Kesisova, I.A., Robinson, B.P., and Spiliotis, E.T. (2021). A septin GTPase scaffold of dynein-dynactin motors triggers retrograde lysosome transport. J Cell Biol *220*.

Khatter, D., Raina, V.B., Dwivedi, D., Sindhwani, A., Bahl, S., and Sharma, M. (2015a). The small GTPase Arl8b regulates assembly of the mammalian HOPS complex on lysosomes. J Cell Sci *128*, 1746-1761.

Khatter, D., Sindhwani, A., and Sharma, M. (2015b). Arf-like GTPase Arl8: Moving from the periphery to the center of lysosomal biology. Cell Logist *5*, e1086501.

Kim, D.I., Jensen, S.C., Noble, K.A., Kc, B., Roux, K.H., Motamedchaboki, K., and Roux, K.J. (2016). An improved smaller biotin ligase for BioID proximity labeling. Mol Biol Cell *27*, 1188-1196.

Klassen, M.P., Wu, Y.E., Maeder, C.I., Nakae, I., Cueva, J.G., Lehrman, E.K., Tada, M., Gengyo-Ando, K., Wang, G.J., Goodman, M., *et al.* (2010). An Arf-like small G protein, ARL-8, promotes the axonal transport of presynaptic cargoes by suppressing vesicle aggregation. Neuron *66*, 710-723.

Korolchuk, V.I., Saiki, S., Lichtenberg, M., Siddiqi, F.H., Roberts, E.A., Imarisio, S., Jahreiss, L., Sarkar, S., Futter, M., Menzies, F.M., *et al.* (2011). Lysosomal positioning coordinates cellular nutrient responses. Nat Cell Biol *13*, 453-460.

Kubala, M.H., Kovtun, O., Alexandrov, K., and Collins, B.M. (2010). Structural and thermodynamic analysis of the GFP:GFP-nanobody complex. Protein Sci *19*, 2389-2401.

Lassen, K.G., McKenzie, C.I., Mari, M., Murano, T., Begun, J., Baxt, L.A., Goel, G., Villablanca, E.J., Kuo, S.Y., Huang, H., *et al.* (2016). Genetic Coding Variant in GPR65 Alters Lysosomal pH and Links Lysosomal Dysfunction with Colitis Risk. Immunity *44*, 1392-1405.

1048 Lee, I.G., Olenick, M.A., Boczkowska, M., Franzini-Armstrong, C., Holzbaur, E.L.F., and
1049 Dominguez, R. (2018). A conserved interaction of the dynein light intermediate chain
1050 with dynein-dynactin effectors necessary for processivity. Nat Commun *9*, 986.

1051 Lee, S., Sato, Y., and Nixon, R.A. (2011). Lysosomal proteolysis inhibition selectively disrupts
1052 axonal transport of degradative organelles and causes an Alzheimer's-like axonal
1053 dystrophy. J Neurosci *31*, 7817-7830.

1054 Levin-Konigsberg, R., Montano-Rendon, F., Keren-Kaplan, T., Li, R., Ego, B., Mylvaganam, S.,
1055 DiCiccio, J.E., Trimble, W.S., Bassik, M.C., Bonifacino, J.S., *et al.* (2019). Phagolysosome
1056 resolution requires contacts with the endoplasmic reticulum and phosphatidylinositol-4-
1057 phosphate signalling. Nat Cell Biol *21*, 1234-1247.

1058 Li, X., Rydzewski, N., Hider, A., Zhang, X., Yang, J., Wang, W., Gao, Q., Cheng, X., and Xu, H.
1059 (2016). A molecular mechanism to regulate lysosome motility for lysosome positioning
1060 and tubulation. Nat Cell Biol *18*, 404-417.

1061 Liu, Y., Kahn, R.A., and Prestegard, J.H. (2009). Structure and membrane interaction of
1062 myristoylated ARF1. Structure *17*, 79-87.

1063 Lord, S.J., Velle, K.B., Mullins, R.D., and Fritz-Laylin, L.K. (2020). SuperPlots: Communicating
1064 reproducibility and variability in cell biology. J Cell Biol *219*.

1065 Lund, V.K., Lycas, M.D., Schack, A., Andersen, R.C., Gether, U., and Kjaerulff, O. (2021). Rab2
1066 drives axonal transport of dense core vesicles and lysosomal organelles. Cell Rep *35*,
1067 108973.

1068 Marwaha, R., Arya, S.B., Jagga, D., Kaur, H., Tuli, A., and Sharma, M. (2017). The Rab7 effector
1069 PLEKHM1 binds Arl8b to promote cargo traffic to lysosomes. J Cell Biol *216*, 1051-1070.

1070 McKenney, R.J., Huynh, W., Tanenbaum, M.E., Bhabha, G., and Vale, R.D. (2014). Activation of
1071 cytoplasmic dynein motility by dynactin-cargo adapter complexes. Science *345*, 337-341.

1072 Men, W., Li, W., Li, Y., Zhao, J., Qu, X., Li, P., and Gong, S. (2019). RUFY3 Predicts Poor
1073 Prognosis and Promotes Metastasis through Epithelial-mesenchymal Transition in Lung
1074 Adenocarcinoma. J Cancer *10*, 6278-6285.

1075 Mori, T., Wada, T., Suzuki, T., Kubota, Y., and Inagaki, N. (2007). Singar1, a novel RUN domain-
1076 containing protein, suppresses formation of surplus axons for neuronal polarity. J Biol
1077 Chem *282*, 19884-19893.

1078 Mrakovic, A., Kay, J.G., Furuya, W., Brumell, J.H., and Botelho, R.J. (2012). Rab7 and Arl8
1079 GTPases are necessary for lysosome tubulation in macrophages. Traffic *13*, 1667-1679.

1080 Nag, S., Rani, S., Mahanty, S., Bissig, C., Arora, P., Azevedo, C., Saiardi, A., van der Sluijs, P.,
1081 Delevoye, C., van Niel, G., *et al.* (2018). Rab4A organizes endosomal domains for sorting
1082 cargo to lysosome-related organelles. J Cell Sci *131*.

1083 Niwa, S., Lipton, D.M., Morikawa, M., Zhao, C., Hirokawa, N., Lu, H., and Shen, K. (2016).
1084 Autoinhibition of a Neuronal Kinesin UNC-104/KIF1A Regulates the Size and Density
1085 of Synapses. Cell Rep *16*, 2129-2141.

1086 Niwa, S., Tao, L., Lu, S.Y., Liew, G.M., Feng, W., Nachury, M.V., and Shen, K. (2017). BORC
1087 Regulates the Axonal Transport of Synaptic Vesicle Precursors by Activating ARL-8.
1088 Curr Biol *27*, 2569-2578 e2564.

1089 Oka, M., Hashimoto, K., Yamaguchi, Y., Saitoh, S.I., Sugiura, Y., Motoi, Y., Honda, K., Kikko, Y.,
1090 Ohata, S., Suematsu, M., *et al.* (2017). Arl8b is required for lysosomal degradation of
1091 maternal proteins in the visceral yolk sac endoderm of mouse embryos. J Cell Sci *130*,
1092 3568-3577.

1093 Palomo-Guerrero, M., Fado, R., Casas, M., Perez-Montero, M., Baena, M., Helmer, P.O.,
1094 Dominguez, J.L., Roig, A., Serra, D., Hayen, H., *et al.* (2019). Sensing of nutrients by
1095 CPT1C regulates late endosome/lysosome anterograde transport and axon growth. Elife
1096 *8*.

1097 Pu, J., Keren-Kaplan, T., and Bonifacino, J.S. (2017). A Ragulator-BORC interaction controls
1098 lysosome positioning in response to amino acid availability. J Cell Biol *216*, 4183-4197.

1099 Pu, J., Schindler, C., Jia, R., Jarnik, M., Backlund, P., and Bonifacino, J.S. (2015). BORC, a
1100 multisubunit complex that regulates lysosome positioning. Dev Cell *33*, 176-188.

1101 Quintyne, N.J., Gill, S.R., Eckley, D.M., Crego, C.L., Compton, D.A., and Schroer, T.A. (1999).
1102 Dynactin is required for microtubule anchoring at centrosomes. J Cell Biol *147*, 321-334.

1103 Raiborg, C., Wenzel, E.M., Pedersen, N.M., Olsvik, H., Schink, K.O., Schultz, S.W., Vietri, M.,
1104 Nisi, V., Bucci, C., Brech, A., *et al.* (2015). Repeated ER-endosome contacts promote
1105 endosome translocation and neurite outgrowth. Nature *520*, 234-238.

1106 Reck-Peterson, S.L., Redwine, W.B., Vale, R.D., and Carter, A.P. (2018). The cytoplasmic dynein
1107 transport machinery and its many cargoes. Nat Rev Mol Cell Biol *19*, 382-398.

Rocha, N., Kuijl, C., van der Kant, R., Janssen, L., Houben, D., Janssen, H., Zwart, W., and Neefjes, J. (2009). Cholesterol sensor ORP1L contacts the ER protein VAP to control Rab7-RILP-p150 Glued and late endosome positioning. J Cell Biol *185*, 1209-1225.

Rosa-Ferreira, C., and Munro, S. (2011). Arl8 and SKIP act together to link lysosomes to kinesin-1. Dev Cell *21*, 1171-1178.

Rosa-Ferreira, C., Sweeney, S.T., and Munro, S. (2018). The small G protein Arl8 contributes to lysosomal function and long-range axonal transport in Drosophila. Biol Open *7*.

Roux, K.J., Kim, D.I., and Burke, B. (2013). BioID: a screen for protein-protein interactions. Curr Protoc Protein Sci *74*, 19 23 11-19 23 14.

Saric, A., Freeman, S.A., Williamson, C., Jarnik, M., Guardia, C.M., Fernandopulle, M.S., Gershlick, D.C., and Bonifacino, J.S. (2021). SNX19 restricts endolysosome motility through contacts with the endoplasmic reticulum. Nat Commun, *in press*.

Schiefermeier, N., Scheffler, J.M., de Araujo, M.E., Stasyk, T., Yordanov, T., Ebner, H.L., Offterdinger, M., Munck, S., Hess, M.W., Wickstrom, S.A., *et al.* (2014). The late endosomal p14-MP1 (LAMTOR2/3) complex regulates focal adhesion dynamics during cell migration. J Cell Biol *205*, 525-540.

Schneider, C.A., Rasband, W.S., and Eliceiri, K.W. (2012). NIH Image to ImageJ: 25 years of image analysis. Nat Methods *9*, 671-675.

Schroeder, C.M., Ostrem, J.M., Hertz, N.T., and Vale, R.D. (2014). A Ras-like domain in the light intermediate chain bridges the dynein motor to a cargo-binding region. Elife *3*, e03351.

Sindhwani, A., Arya, S.B., Kaur, H., Jagga, D., Tuli, A., and Sharma, M. (2017). Salmonella exploits the host endolysosomal tethering factor HOPS complex to promote its intravacuolar replication. PLoS Pathog *13*, e1006700.

Steffan, J.J., Dykes, S.S., Coleman, D.T., Adams, L.K., Rogers, D., Carroll, J.L., Williams, B.J., and Cardelli, J.A. (2014). Supporting a role for the GTPase Rab7 in prostate cancer progression. PLoS One *9*, e87882.

Sztul, E., Chen, P.W., Casanova, J.E., Cherfils, J., Dacks, J.B., Lambright, D.G., Lee, F.S., Randazzo, P.A., Santy, L.C., Schurmann, A., *et al.* (2019). ARF GTPases and their GEFs and GAPs: concepts and challenges. Mol Biol Cell *30*, 1249-1271.

Terawaki, S., Camosseto, V., Prete, F., Wenger, T., Papadopoulos, A., Rondeau, C., Combes, A., Rodriguez Rodrigues, C., Vu Manh, T.P., Fallet, M., *et al.* (2015). RUN and FYVE domain-containing protein 4 enhances autophagy and lysosome tethering in response to Interleukin-4. J Cell Biol *210*, 1133-1152.

Tsuruta, F., and Dolmetsch, R.E. (2015). PIKfyve mediates the motility of late endosomes and lysosomes in neuronal dendrites. Neurosci Lett *605*, 18-23.

Tuli, A., Thiery, J., James, A.M., Michelet, X., Sharma, M., Garg, S., Sanborn, K.B., Orange, J.S., Lieberman, J., and Brenner, M.B. (2013). Arf-like GTPase Arl8b regulates lytic granule polarization and natural killer cell-mediated cytotoxicity. Mol Biol Cell *24*, 3721-3735.

Vilela, F., Velours, C., Chenon, M., Aumont-Nicaise, M., Campanacci, V., Thureau, A., Pylypenko, O., Andreani, J., Llinas, P., and Menetrey, J. (2019). Structural characterization of the RH1-LZI tandem of JIP3/4 highlights RH1 domains as a cytoskeletal motor-binding motif. Sci Rep *9*, 16036.

Vukmirica, J., Monzo, P., Le Marchand-Brustel, Y., and Cormont, M. (2006). The Rab4A effector protein Rabip4 is involved in migration of NIH 3T3 fibroblasts. J Biol Chem *281*, 36360-36368.

Vukoja, A., Rey, U., Petzoldt, A.G., Ott, C., Vollweiter, D., Quentin, C., Puchkov, D., Reynolds, E., Lehmann, M., Hohensee, S., *et al.* (2018). Presynaptic Biogenesis Requires Axonal Transport of Lysosome-Related Vesicles. Neuron *99*, 1216-1232 e1217.

Wang, G., Zhang, Q., Song, Y., Wang, X., Guo, Q., Zhang, J., Li, J., Han, Y., Miao, Z., and Li, F. (2015). PAK1 regulates RUFY3-mediated gastric cancer cell migration and invasion. Cell Death Dis *6*, e1682.

Wei, Z., Sun, M., Liu, X., Zhang, J., and Jin, Y. (2014). Rufy3, a protein specifically expressed in neurons, interacts with actin-bundling protein Fascin to control the growth of axons. J Neurochem *130*, 678-692.

Willett, R., Martina, J.A., Zewe, J.P., Wills, R., Hammond, G.R.V., and Puertollano, R. (2017). TFEB regulates lysosomal positioning by modulating TMEM55B expression and JIP4 recruitment to lysosomes. Nat Commun *8*, 1580.

Xie, R., Wang, J., Tang, W., Li, Y., Peng, Y., Zhang, H., Liu, G., Huang, X., Zhao, J., Li, A., *et al.* (2017). Rufy3 promotes metastasis through epithelial-mesenchymal transition in colorectal cancer. Cancer Lett *390*, 30-38.

Zhu, H., Dai, W., Li, J., Xiang, L., Wu, X., Tang, W., Chen, Y., Yang, Q., Liu, M., Xiao, Y., *et al.* (2019). HOXD9 promotes the growth, invasion and metastasis of gastric cancer cells by transcriptional activation of RUFY3. J Exp Clin Cancer Res *38*, 412.

Fig. 1

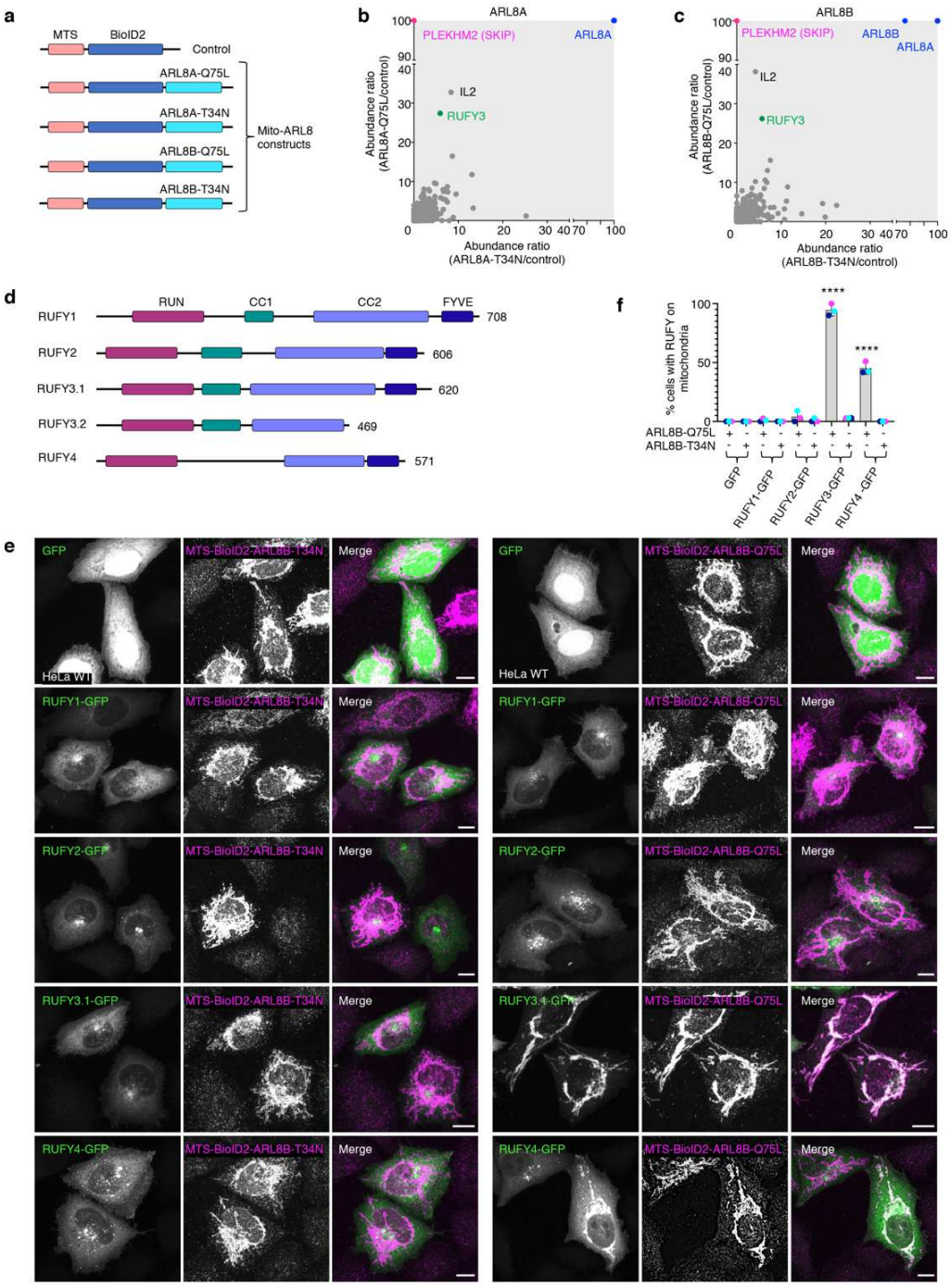

Fig. 1: Identification of RUFY3 and RUFY4 as ARL8 effectors.

a Schematic representation of control and Mito-ARL8 constructs used in MitoID. MTS: mitochondrial-targeting sequence from TOM20 (Kanaji et al., 2000); BioID2: humanized *A. aeolicus* biotin ligase (Kim et al., 2016). Constructs were expressed in HEK293T cells. **b** Graph showing the abundance of mass spectrometry hits identified for MTS-BioID2-ARL8A-Q75L/MTS-BioID2 control *vs.* MTS-BioID2-ARL8A-T34N/MTS-BioID2 control using MitoID. **c** Same as b for MTS-BioID2-ARL8B-Q75L/MTS-BioID2 control *vs.* MTS-BioID2-ARL8B-T34N/MTS-BioID2 control. Hits of interest in panels b and c are highlighted in color. **d** Domain organization of RUFY proteins in N- to C-terminal direction. RUN: RPIP8, UNC-14 and NESCA domain, CC1: coiled-coil 1 domain, CC2: coiled-coil 2 domain, FYVE: Fab1, YOTB, Vac1 and EEA1 domain. Amino-acid numbers are indicated. RUFY3.1 and RUFY3.2 are two spliceforms of RUFY3. **e** Immunofluorescence microscopy of HeLa cells co-expressing GFP or RUFY-GFP fusion proteins (green) together with MTS-BioID2-ALR8B-Q75L or -T34N. Fixed cells were stained with antibody to BioID2 (magenta), and imaged by confocal microscopy. Single channels are shown in grayscale. Scale bars: 10 μm. **e** Quantification of the percentage of cells in which RUFY proteins were re-localized to mitochondria from experiments such as that in panel e (n=3 independent experiments; minimum of 300 cells per condition). Statistical significance was calculated using one-way ANOVA with multiple comparisons to the GFP control using Dunnett's test, **** $p<0.0001$. See also Supplementary Fig. 1 and Supplementary Dataset 1.

Fig. 2

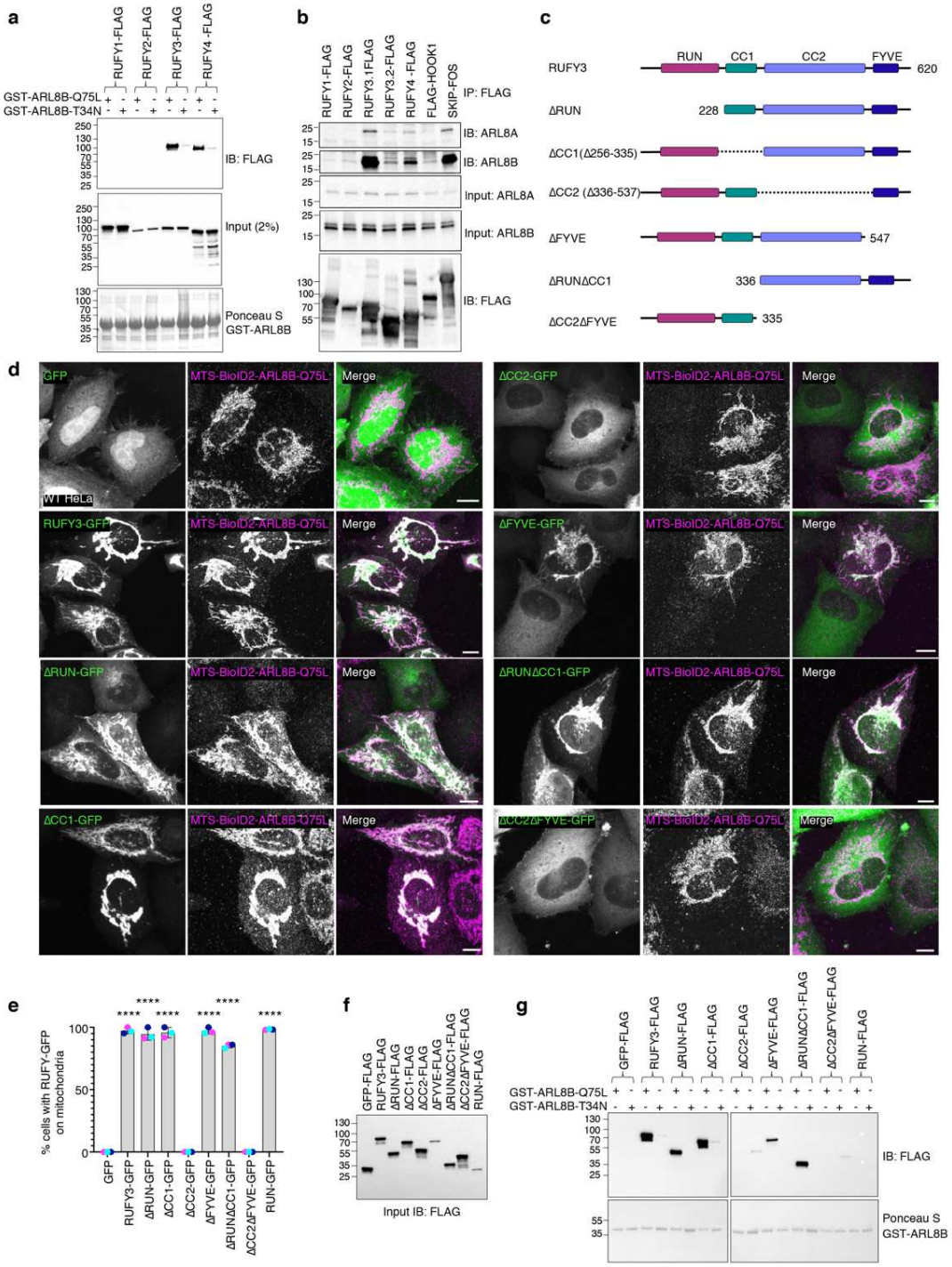

Fig. 2: Biochemical evidence for the binding of RUFY3 and RUFY4 to ARL8 and dissection of RUFY3 domains required for ARL8 binding.

a Recombinant GST-ARL8B-Q75L and -T34N were purified using the GST tag and used to pull down the indicated RUFY-FLAG proteins expressed by transfection in HEK293T cells. GST proteins were detected by Ponceau S staining. IB: immunoblotting. **b** Extracts of HEK293T cells transfected with plasmids encoding the indicated FLAG- or FOS-tagged proteins were immunoprecipitated (IP) with anti-FLAG, and immunoblotted (IB) for endogenous ARL8A and ARL8B and the FLAG tag. In both panel a and b, the positions of molecular mass markers (in kDa) are indicated at left. Both experiments are representative of two experiments with similar results. **c** Schematic representation of RUFY3 deletion constructs. Domain organization is as depicted in Fig. 1b. Amino-acid numbers are indicated. Δ stands for deletion. **d** Immunofluorescence microscopy of HeLa cells expressing GFP or the RUFY3-GFP deletion constructs shown in panel c (green) together with MTS-BioID2-ALR8B-Q75L. Fixed cells were stained with antibody to BioID2 (magenta). Single channels are shown in grayscale. Scale bars: 10 μm. **e** Quantification of the percentage of cells in which RUFY-GFP proteins were re-localized to mitochondria (n=3 independent experiments; minimum of 300 cells per condition) from experiments such as that shown in panel d. Statistical significance compared to cells expressing GFP was calculated using one-way ANOVA with multiple comparisons with Dunnett's test. **** $p<0.0001$. **f,g** Recombinant GST-ARL8B-Q75L and -T34N were purified using the GST tag and used to pull down RUFY3-FLAG deletion constructs expressed by transfection in HEK293T cells. FLAG-tagged proteins in the input (f) and pull downs (g) were detected by immunoblotting (IB) for the FLAG epitope. Input GST-ARL8B-Q75L and -T34N were detected by Ponceau-S staining. The positions of molecular mass markers (in kDa) in panels f and g are indicated at left. This experiment is representative of two experiments with similar results.

Fig. 3

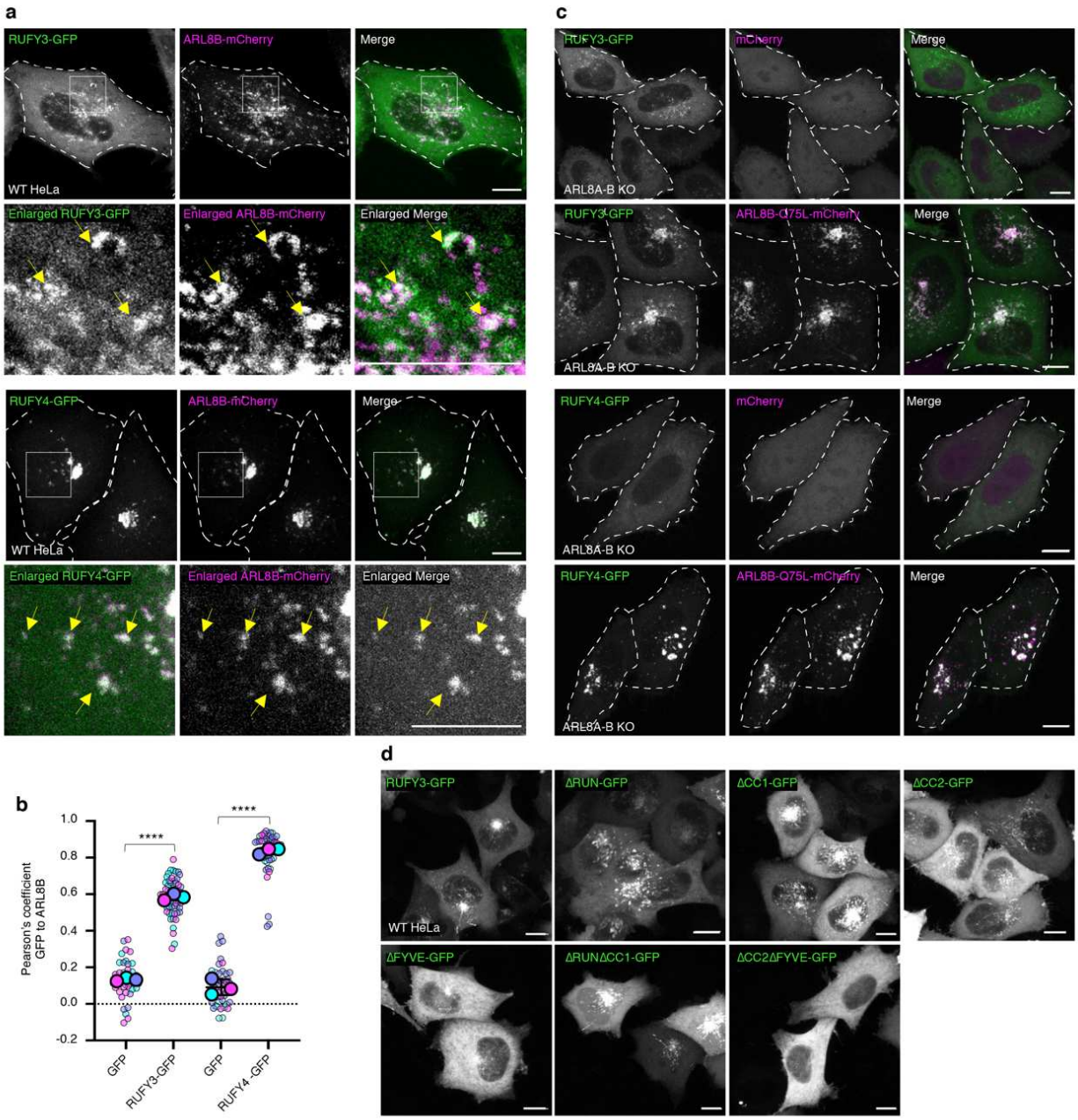

Fig. 3: ARL8 recruits RUFY3 and RUFY4 to a cluster of juxtanuclear vesicles.

a Live-cell imaging of HeLa cells co-expressing RUFY3-GFP or RUFY4-GFP (green) with ARLB-mCherry (magenta). Cell edges are outlined by dashed lines. Scale bars: 10 µm. The lower rows are 4.7-fold (RUFY3) and 3.7-fold (RUFY4) enlargements of the boxed areas. Arrows indicate vesicles where RUFY-GFP proteins and ARLB-mCherry co-localize. Single channels are shown

in grayscale. **b** Co-localization of GFP (control), RUFY3-GFP or RUFY4-GFP with ARL8B-mCherry from experiments such as that in panel a. The graph shows the mean ± SD and the individual data points from 3 independent experiments. Statistical significance was calculated using Student's t-test. **** $p<0.0001$. **c** ARL8A-B-KO cells were co-transfected with plasmids encoding RUFY3-GFP or RUFY4-GFP (green) with mCherry (control) or ARL8B-Q75L-mCherry (magenta). Cells were imaged live by confocal microscopy. Single channels are shown in grayscale. Scale bars: 10 μm. **d** Live-cell imaging of HeLa cells expressing the RUFY3-GFP deletion constructs shown in Fig. 2c. Images are in grayscale. Scale bars: 10 μm.

Fig. 4

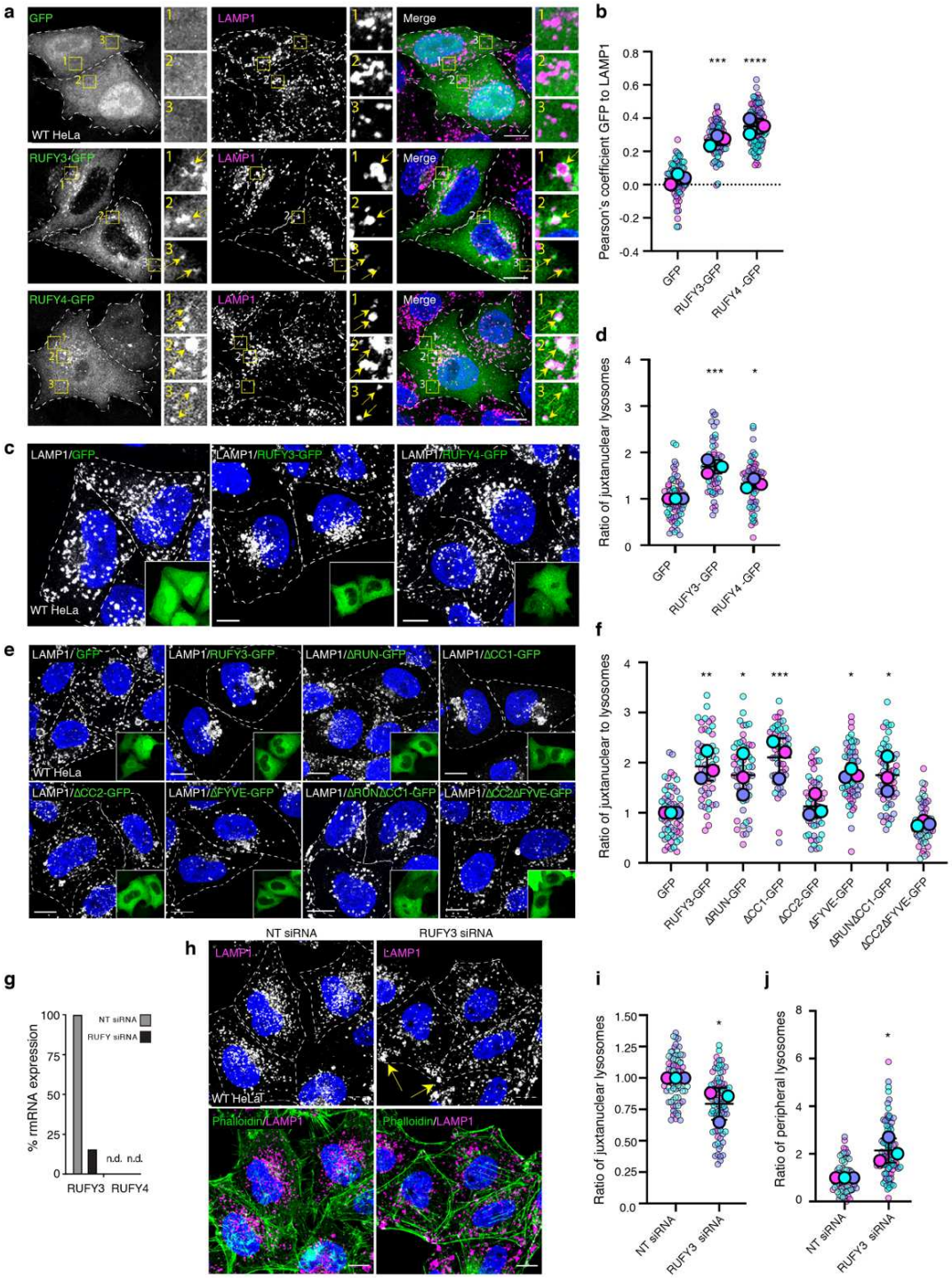

Fig. 4: RUFY3 and RUFY4 promote juxtanuclear localization of lysosomes.

a Co-localization of RUFY3-GFP or RUFY4-GFP with endogenous LAMP1. Immunofluorescence microscopy of HeLa cells transfected with plasmids expressing GFP (control), RUFY3-GFP or RUFY4-GFP (green), fixed and immunostained for endogenous LAMP1 (magenta). Nuclei were stained with DAPI (blue). Cell edges are outlined by dashed lines. Scale bars: 10 μm. Insets show 3-fold enlargements of the boxed areas. Single channels are shown in grayscale. Arrows indicate vesicles where RUFY-GFP proteins co-localize with LAMP1. **b** Co-localization of GFP, RUFY3-GFP or RUFY4-GFP with endogenous LAMP1 from experiments such as that in a. The graph shows the mean ± SD from and the individual data points from 3 independent experiments. Statistical significance was calculated using one-way ANOVA with multiple comparisons to the GFP control using Dunnett's test. *** $p<0.001$, **** $p<0.0001$. **c** Overexpression of RUFY3-GFP or RUFY4-GFP causes juxtanuclear clustering of lysosomes. This experiment was done as described for panel a. Endogenous LAMP1 staining is shown in grayscale and GFP images in green (inset). Nuclei were stained with DAPI (blue). Cell edges are outlined by dashed lines. Scale bars: 10 μm. **d**, Quantification of the ratio of juxtanuclear LAMP1 to total LAMP1 calculated by shell analysis from experiments such as those in panels a and b. The graph shows the mean ± SD and the individual data points from 3 independent experiments. Statistical significance was calculated using one-way ANOVA with multiple comparison to the GFP control using Dunnett's test. * $p<0.05$, *** $p<0.001$. **e** Immunofluorescence microscopy of HeLa cells transfected with GFP (control) or RUFY3-GFP deletions constructs depicted in Fig. 2c (green in the insets), fixed and immunostained for endogenous LAMP1 (grayscale). Nuclei were stained with DAPI (blue). Cell edges are outlined by dashed lines. Scale bars: 10 μm. **f** Quantification, as described for panel d, of the effect of RUFY3-GFP deletion constructs on the distribution of LAMP1 from 3 independent experiments such as that shown in panel d. Statistical significance was calculated using one-way ANOVA with multiple comparisons to GFP using Dunnett's test. * $p<0.05$, ** $p<0.01$, *** $p<0.001$. **g** qRT-PCR of mRNA expression of RUFY3 and RUFY4 relative to actin in HeLa cells treated with non-targeting (NT) or RUFY3/4 siRNAs. n.d., not detected. **h** Immunofluorescence microscopy of HeLa cells treated with non-targeting (NT) or RUFY3 siRNA and stained with antibodies to endogenous LAMP1 (grayscale and magenta) and Alexa fluor 546-conjugated phalloidin (green) to highlight cell edges. Nuclei were stained with DAPI (blue). Cell edges are outlined by dashed lines. Scale bars: 10 μm. **i** Quantification, as described for panel d, of the effect of NT or RUFY3 siRNA on the juxtanuclear localization of LAMP1 from 3 independent experiments such as that shown in panel h. **j** Quantification of the ratio of peripheral LAMP1 to total LAMP1 calculated by shell analysis from 3 independent experiments such as that shown in panel h.

Fig. 5

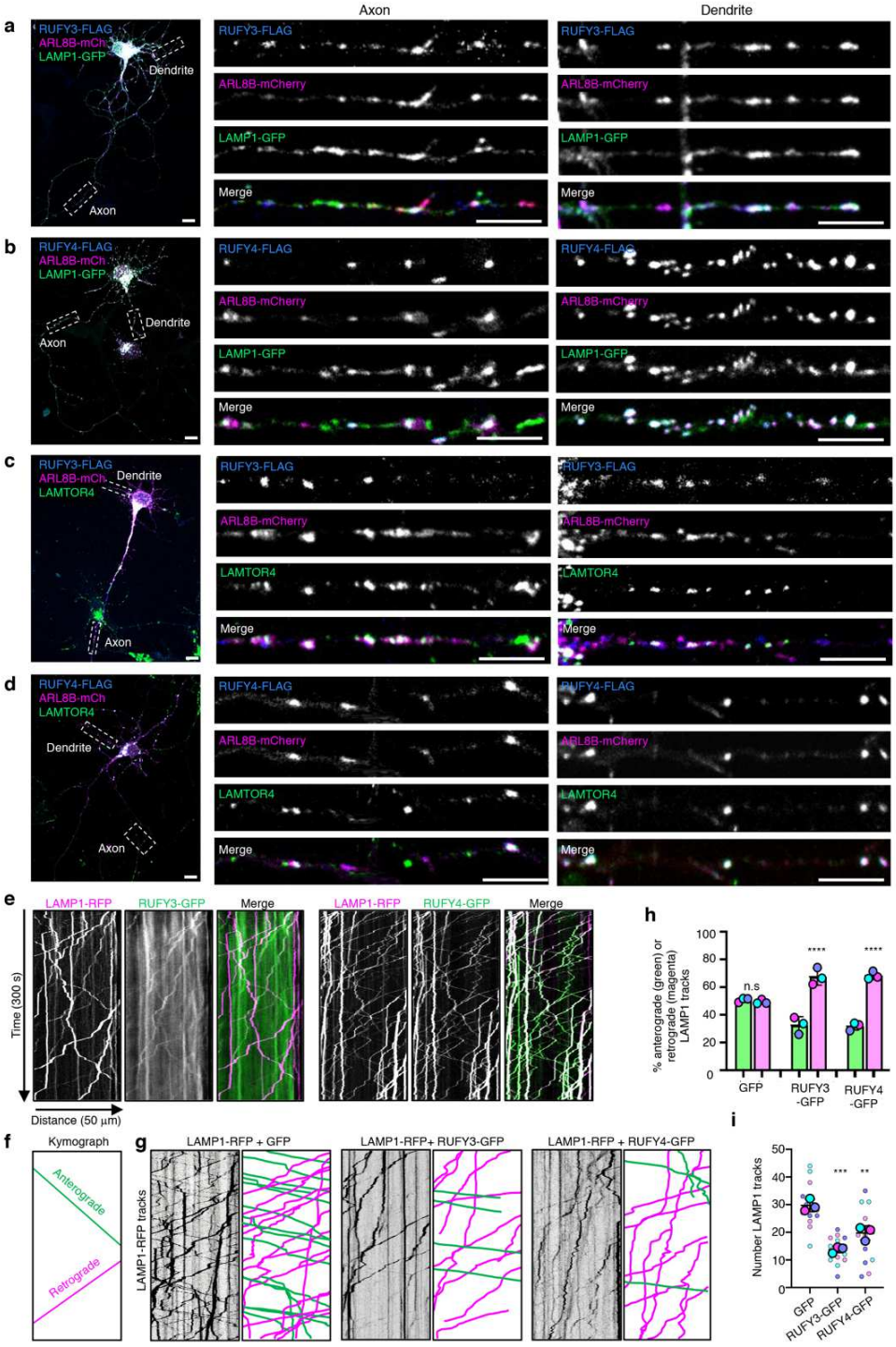

Fig. 5: RUFY3 and RUFY4 promote axonal retrograde transport.

a,b Immunofluorescence microscopy of rat hippocampal neurons transfected with plasmids encoding RUFY3-FLAG (a) or RUFY4-FLAG (b) along with ARL8B-mCherry and LAMP1-GFP. Neurons were fixed, permeabilized and RUFY-FLAG proteins were detected by immunostaining with antibody to the FLAG epitope (blue), and ARL8B-mCherry (magenta) and LAMP1-GFP (green) by their intrinsic fluorescence. Images on the left show neurons (Scale bars: 10 μm) with boxes indicating axons and dendrites that are enlarged on the right (Scale bars: 5 μm). **c,d** Same as panels a and b, but neurons were immunostained with antibody to endogenous LAMTOR4 (green) instead of imaged for LAMP1-GFP. **e** Rat hippocampal neurons were transfected with plasmids encoding LAMP1-RFP (magenta) along with RUFY3-GFP or RUFY4-GFP (green), axons were imaged live by spinning-disk confocal microscopy, and trajectories of fluorescent particles were represented as kymographs. Single channels are represented in grayscale. **f** Lines with negative or positive slopes in the kymographs correspond to vesicles moving in anterograde (green) or retrograde (magenta) directions, respectively. **g** Kymographs representing the movement of LAMP1-RFP (grayscale) in live cells co-expressing GFP, RUFY3-GFP or RUFY4-GFP (not shown), with manual analysis of the tracks according to the convention in panel f. **h** Quantification of the percentage of anterograde (green) and retrograde (magenta) movement of LAMP1-RFP vesicles in neurons expressing GFP, RUFY3-GFP or RUFY4-GFP from experiments such as that in panel g. Values are the mean ± SD from 3 independent experiments with a total of 15 neurons analyzed per condition and counting a total of 445 (GFP), 206 (RUFY3-GFP), 282 (RUFY4-GFP) LAMP1-RFP motile events per condition. Statistical significance was calculated using one-way ANOVA with multiple comparisons using Tukey's test. **** $p<0.0001$; n.s., not significant. **i** Quantification of the total number of LAMP1-RFP tracks in neurons expressing GFP, RUFY3-GFP or RUFY4-GFP from experiments such as that in panel g. The graph shows the mean ± SD and the individual data points from 3 independent experiments. Statistical significance was calculated using one-way ANOVA with multiple comparisons to the GFP control using Dunnett's test. *** $p<0.001$, ** $p<0.01$. See also Supplementary Movie 1.

Fig. 6

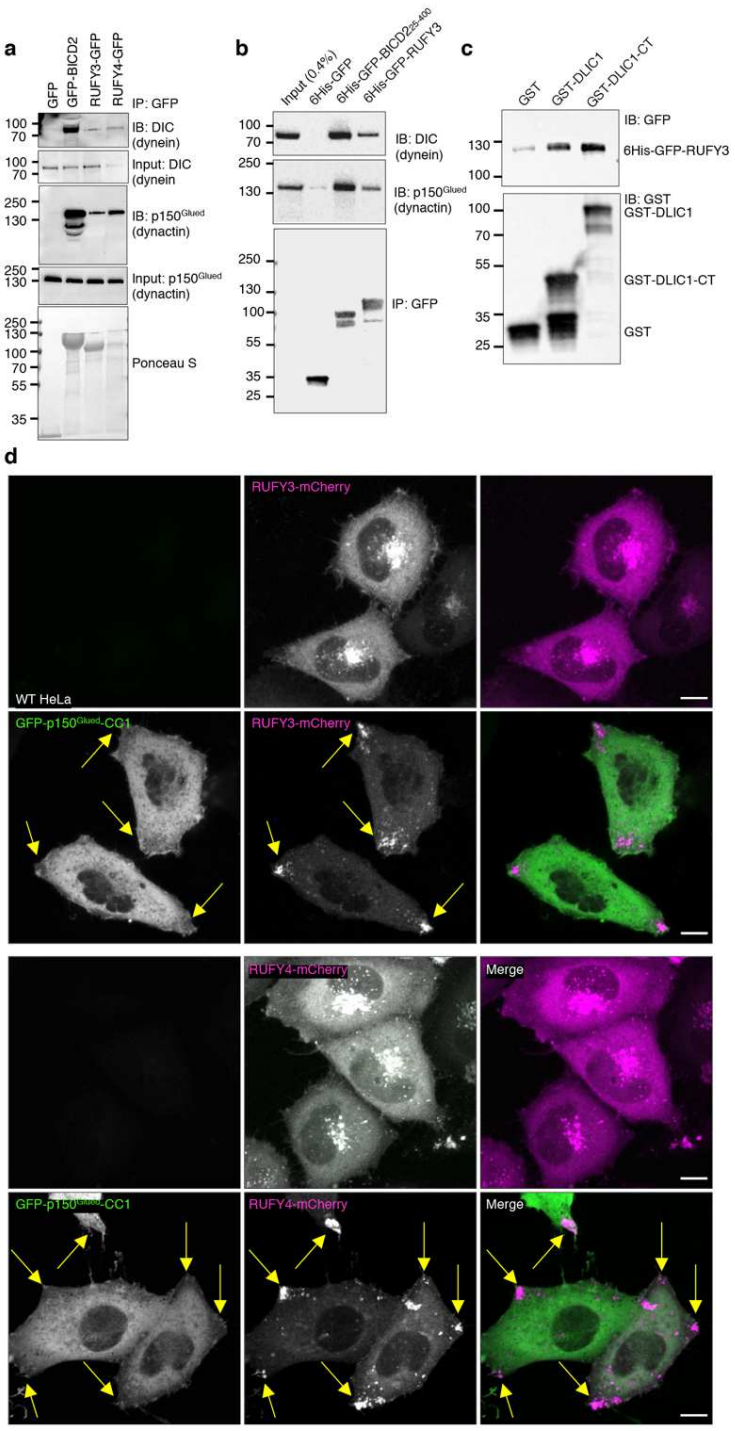

Fig. 6: RUFY3 and RUFY4 bind dynein-dynactin.

a HEK293T cells were transfected with plasmids encoding GFP (negative control), GFP-BICD2 (positive control), RUFY3-GFP or RUFY4-GFP. Cell extracts were analyzed by

immunoprecipitation (IP) with antibody to GFP followed by immunoblotting for endogenous dynein intermediate chain (DIC) and the endogenous $p150^{Glued}$ subunit of dynactin. Ponceau S staining shows the levels of immunoprecipitated GFP-tagged proteins. The experiment shown in this panel is one of two with similar results. **b** Extracts of HEK293T cells were incubated with recombinant 6His-Strep-GFP (negative control), His6-Strep-GFP-$BICD2_{25-400}$ (positive control) or 6His-Strep-GFP-RUFY3, pulled down with Strep-Tactin agarose, and immunoblotted for endogenous dynein intermediate chain (DIC), the endogenous $p150^{Glued}$ of dynactin, or GFP. The GFP used to make these constructs is a variant named sfGFP, for super-folder GFP. The experiment shown in this panel is one of two with similar results. **c** Glutathione-Sepharose preloaded with purified, recombinant GST (negative control), GST-DLIC1 or GST-DLIC1-CT (C-terminal domain) were incubated with purified, recombinant 6His-sfGFP-RUFY3. Bound proteins were detected by immunoblotting with antibodies to GFP and GST. The positions of molecular mass markers (in kDa) in panels a-c are indicated at left. **d** Live-cell imaging of HeLa cells co-expressing RUFY3-mCherry or RUFY4-mCherry (magenta) without or with GFP-$p150^{Glued}$-CC1 (green). Single channel images are shown in grayscale. Scale bars: 10 μm. Arrows point to RUFY proteins at cell tips. This experiment is one of two with similar results.

Fig. 7

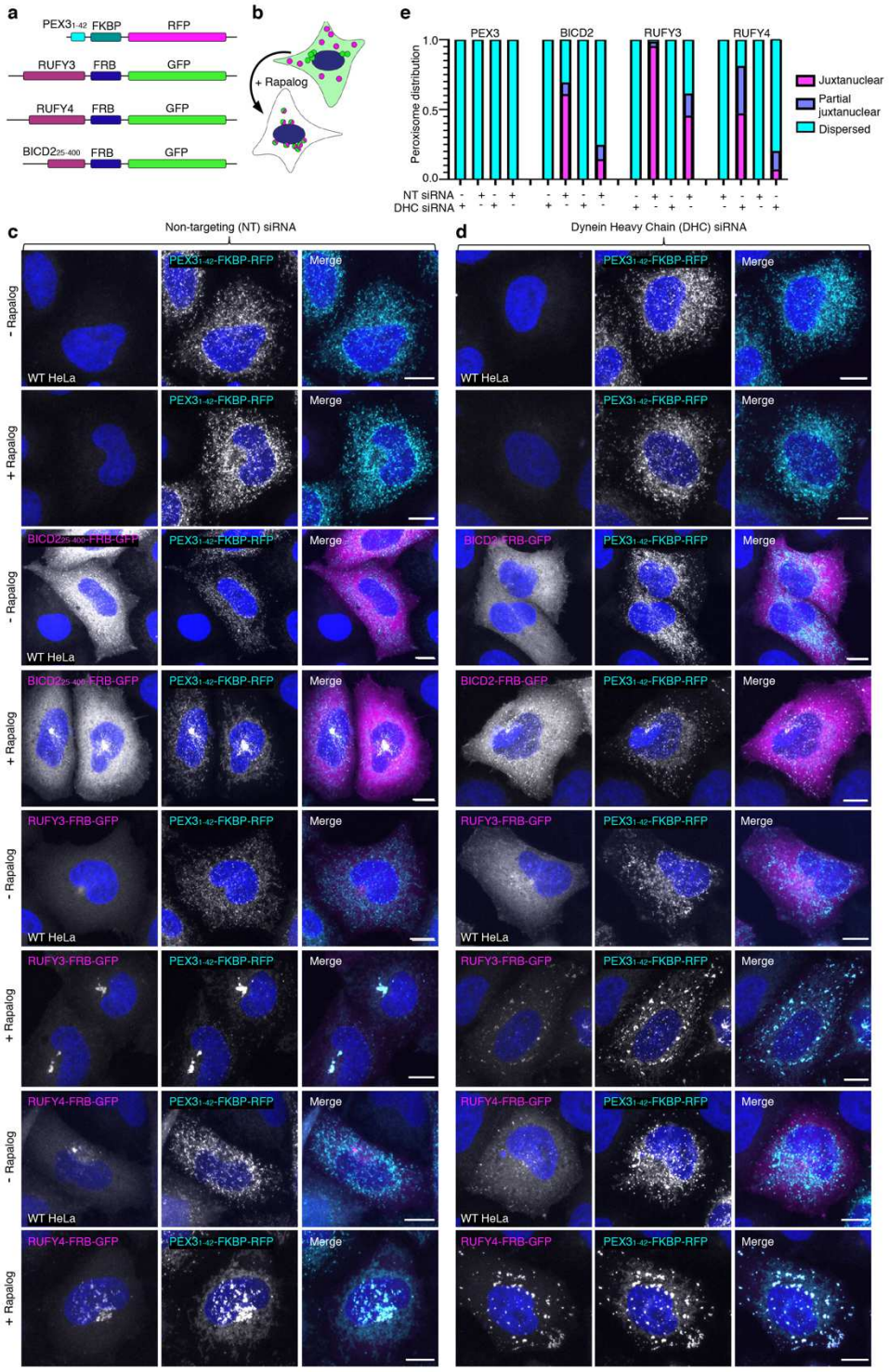

Fig. 7: Targeting of RUFY3 and RUFY4 to peroxisomes promotes their juxtanuclear accumulation in a dynein-dependent manner.

a Schematic representation of constructs used in the peroxisome re-localization assay. $PEX3_{1-42}$: peroxisomal-targeting signal from PEX3; FKBP: FK506-binding protein; FRB: FKBP rapamycin binding. Constructs are represented in the N- to C-terminal direction. $BICD2_{25-400}$ was used as a positive control for a dynein-dynactin adaptor. FKBP binds to FRB upon addition of rapalog. **b** Schematic representation of the rapalog-induced juxtanuclear re-localization of peroxisomes labeled by $PEX3_{1-42}$-FKBP-RFP (magenta) by a hypothetical dynein-dynactin adaptor fused to FRB and GFP (green). **c,d** Fluorescence microscopy of HeLa cells treated with non-targeting (NT) siRNA (c) or dynein heavy chain (DHC) siRNA (d), co-transfected with plasmids encoding the indicated proteins, and incubated for 1 h without (-) or with (+) 0.5 μM rapalog. Nuclei were stained with DAPI. Scale bars: 10 μm. This experiment is representative of 3 experiments with similar results. **e** Cells from experiments such as that shown in panels c and d (a minimum of 200 cells from 2-3 independent experiments) were visually scored for the distribution of peroxisomes.

Fig. 8

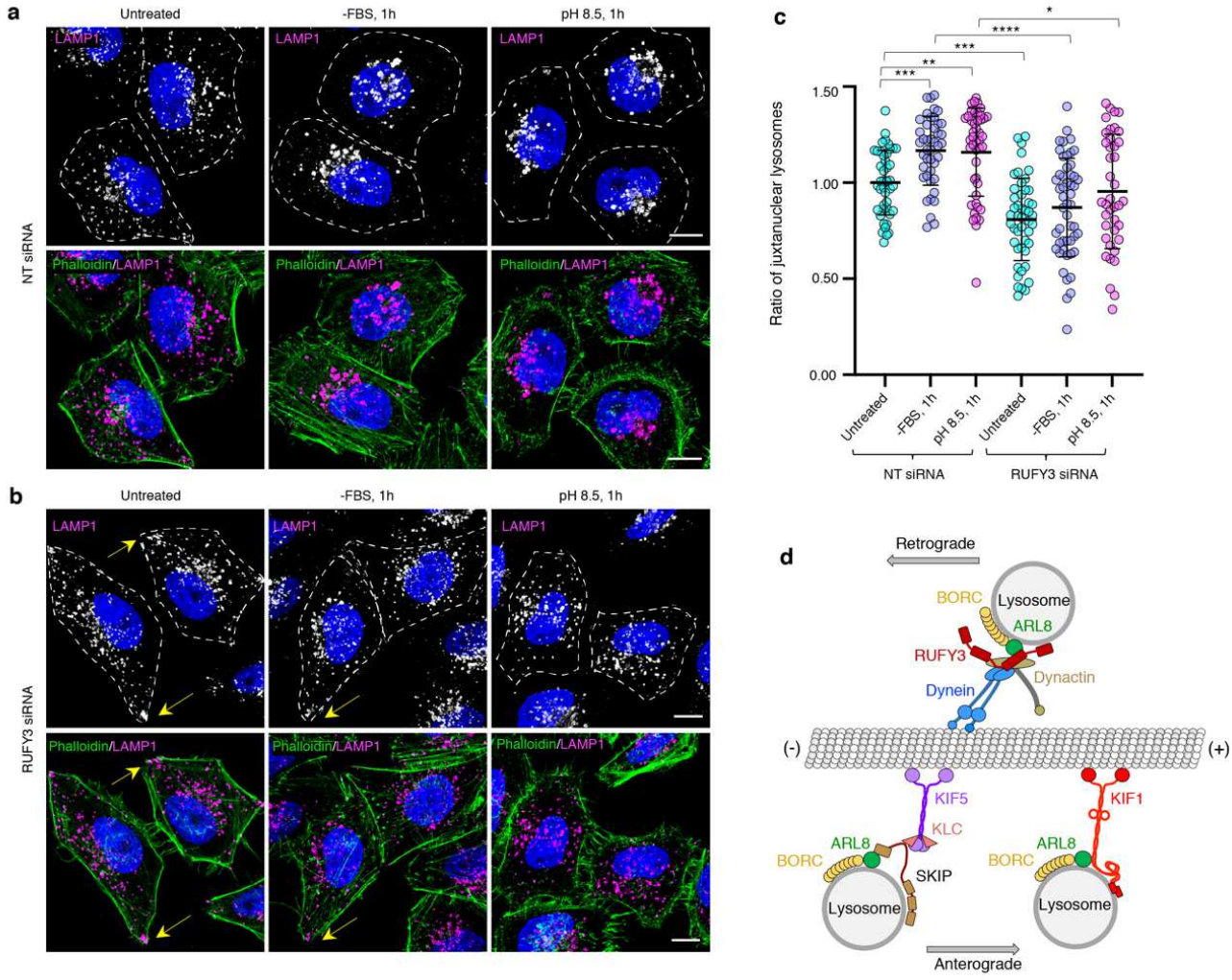

Fig. 8: RUFY3 is required for juxtanuclear clustering of lysosomes induced by serum starvation cytoplasmic alkalinization.

a,b HeLa cells were treated with non-targeting (**a**) or RUFY3 siRNA (**b**) for 96 h, and incubated for 1 h at 37 °C in serum-free DMEM or for 1 h in regular culture medium adjusted to pH 8.5, as indicated in the figure. Cells were then fixed, permeabilized and immunostained with antibody to endogenous LAMP1 (grayscale and magenta) and Alexa Fluor 546-conjugated phalloidin (green). Nuclei were stained with DAPI (blue). Arrows indicate accumulation of lysosomes at cell tips caused by RUFY3 depletion. Scale bars: 10 μm. **c** Quantification of the ratio of juxtanuclear LAMP1 to total LAMP1 calculated by shell analysis from the experiment shown in

panels a and b, normalized to untreated cells in regular culture medium. The graph shows the mean ± SD and the individual values from 40-50 cells analyzed per condition. Statistical significance was calculated by Brown-Forsythe and Welch ANOVA tests with multiple comparisons using Dunnett's T3 test. **** $p<0.0001$, *** $p<0.001$, ** $p<0.01$, ** $p<0.05$. **d** Schematic representation of the role of ARL8 in regulating both retrograde or anterograde of lysosomes through interactions with different effectors. BORC promotes recruitment of ARL8 to lysosomes (Pu et al., 2015). In turn, ARL8 recruits RUFY3 (or RUFY4), which serves as an adaptor for dynein-dynactin, thus driving transport from the plus to the minus end of microtubules (*i.e.*, retrograde transport) (this study). Alternatively, ARL8 recruits kinesin-1 ($KIF5_2$-KLC_2) via SKIP or kinesin-3 (KIF1) directly, driving transport from the minus to the plus end of microtubules (Farias et al., 2017; Guardia et al., 2016; Pu et al., 2015; Rosa-Ferreira and Munro, 2011).

Supplementary Fig. 1

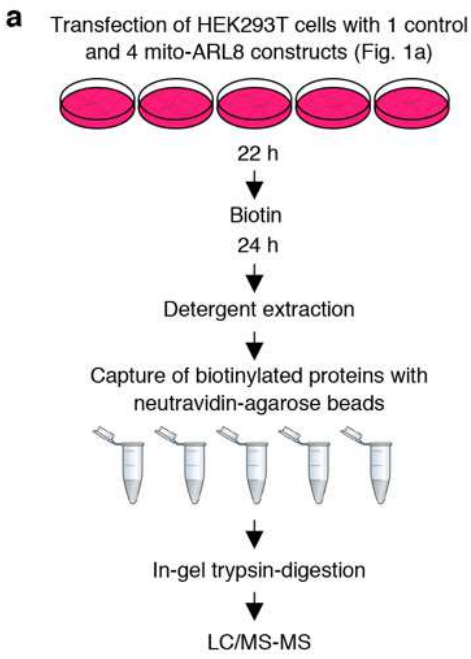

b

RUFY3.1 peptides	Amino acids
[R].ELDDISLTPDPEPTHEDPNYLMANER.[M]	44-69
[K].QDFGDKINSLQLEVEELTR.[Q]	466-484
[K].INSLQLEVEELTR.[Q]	472-484
[R].NQLELELK.[Q]	487-494
[R].LQPHPMDEQDQLLLSEKPQLCQLCQEDGSLTK.[N]	542-573
[K].NCSGTFCDACSTNELPLPSSIK.[L]	578-599

c

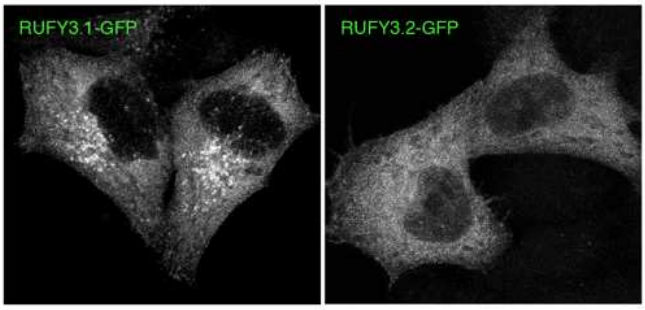

Supplementary Fig. 1: MitoID procedure and identification of RUFY3.1.
a Workflow of the MitoID procedure. **b** Peptides and amino-acid numbers specific for the RUFY3.1 spliceform identified by mass spectrometry. **b** Confocal microscopy of HeLa cells transfected with plasmids encoding RUFY3.1-GFP or RUFY3.2-GFP. Scale bars: 10 µm. Notice that RUFY3.1-GFP associates with vesicles, whereas RUFY3.2-GFP is cytosolic.

Supplementary Dataset 1: List of proteins identified in the MitoID mass spectrometry
A-TN: Mito-BioID2-ARL8A-T34N, A-QL: Mito-BioID2-ARL8A-Q75L, B-TN: Mito-BioID2-ARL8B-T34N. B-QL: Mito-BioID2-ARL8B-Q75L. Ctrl: MitoID-BioID2 control.

Supplementary Movie M1: RUFY3 and RUFY4 co-move with LAMP1 labeled lysosomes in the axon.
DIV5 rat hippocampal neurons co-expressing LAMP1-RFP with RUFY3-GFP or RUFY4-GFP were imaged using a spinning-disk confocal microscopy. Dual-color images of 50 μm adjacent to the axon initial segment (AIS) at a speed of 15 frame per second for 300 seconds without any delay. Notice the co-movement of LAMP1-RFP with RUFY3-GFP or RUFY4-GFP.

Supplementary Files

This is a list of supplementary files associated with this preprint. Click to download.

- SupplementaryDataset1.xlsx
- Supplementarymovie1.mov